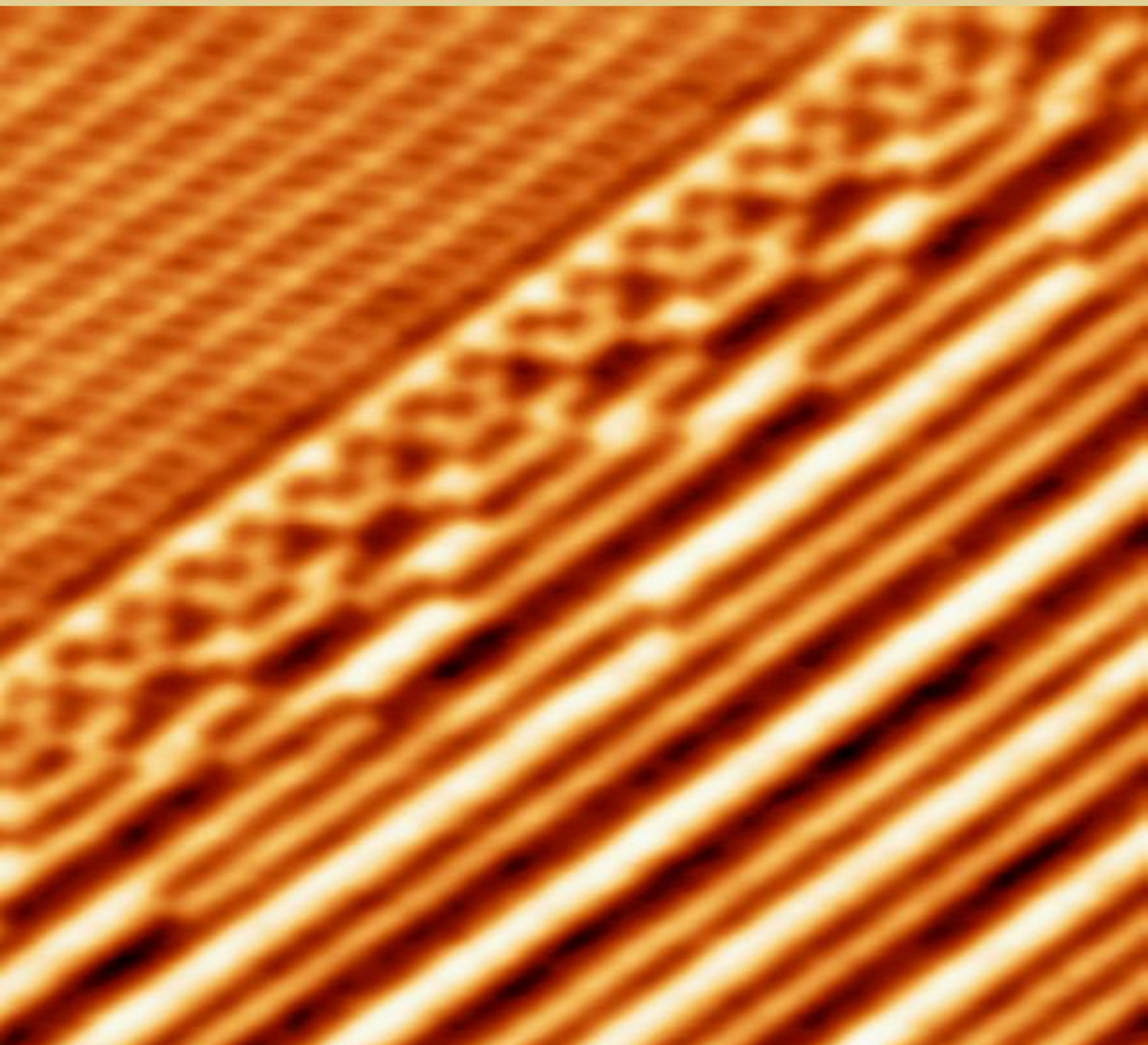


Volume 4, Number 1

December 2022

Nanomaterials Science & Engineering



Volume 4, Number 1

December 2022

Nanomaterials Science & Engineering

Title

Nanomaterials Science & Engineering (NMS&E), Vol.4, No.1, 2022

Editors-in-Chief

Igor Bdikin
Paula Alexandrina de Aguiar Pereira Marques
Duncan Paul Fagg
Gil Gonçalves

Editorial Board

Alexander Titov, Andrei Kovalevsky, António Manuel de Amaral Monteiro Ramos, António Manuel de Bastos Pereira, António Manuel Godinho Completo, Bagautdinov Bagautdin, Binay Kumar, Budhendra Singh, Cicero R. Cena, D. Pukazhselvan, Dmitry A. Kiselev, Dmitry Karpinsky, Eudes Borges de Araujo, Gil Gonçalves, Gonzalo Guillermo Otero Irurueta, Indrani Coondoo, João Paulo Davim Tavares da Silva, José Coutinho, Maciej Wojtas, Manoj Kumar Singh, Margarida Isabel Cabrita Marques Coelho, Maxim Silibin, Münir Tasdemir, Neeraj Panwar, Nikolai Sobolev, Oleksandr Tkach, Paula Celeste da Silva Ferreira, Philip Leduc, Radheshyam Rai, Sergey Bozhko, Svitlana Kopyl, Vincent Ball, Vítor António Ferreira da Costa, Vladimir Bystrov, Yuri Dekhtyar

Editorial Managers

Igor Bdikin
Gil Gonçalves
Raul Simões

Cover and Logo

Igor Bdikin (Laptop Hard Disk, Magnetic Force Microscopy image (MFM), 3.0x3.0 μm^2)

Publisher

University of Aveiro

Support

Serviços de Biblioteca, Informação Documental e Museologia
Centre for Mechanical Technology & Automation (TEMA)
Mechanical Engineering Department
University of Aveiro

Copyright Information

All work licensed under Creative Commons Attribution License that allows others to share the work with an acknowledgement of the work's authorship and initial publication in this journal. Copyrights to illustrations published in the journal remain with their current copyright holders. It is the author's responsibility to obtain permission to quote from copyright sources.

Mailing Address

Department of Mechanical Engineering
University of Aveiro
Aveiro 3810-193
Portugal
E-mail: bdikin@ua.pt

ISSN: 2184-7002

Indrani Coondoo Synthesis and characterization of multiferroic magnetoelectric ceramic composites	5-9
Gunnar Suchaneck Tunnel magnetoresistance of granular superparamagnetic and ferrimagnetic structures	10-20
Lynda Djoudi, Belkis Bourmal and Mahmoud Omari Synthesis and structural Characterization of Cu Substituted SrCoO_{3-δ} Perovskite Oxides	21-26
Felipe Teixeira Mabilia, Shu Hui Wang Conductivity and transmittance enhancement of PEDOT:PSS thin films by graphene addition	27-37

Synthesis and characterization of multiferroic magnetoelectric ceramic composites

Indrani Coondoo

Department of Physics & CICECO-Aveiro Institute of Materials, University of Aveiro, Aveiro 3810-193, Portugal

Corresponding author, e-mail address: indrani.coondoo@ua.pt

Received 1 September 2022; accepted 16 November 2022; published online 20 December 2022

ABSTRACT

Ceramic composites with composition $(1-x)[\text{Ba}_{0.85}\text{Ca}_{0.15}\text{Zr}_{0.1}\text{Ti}_{0.9}\text{O}_3] - x[\text{Ni}_{0.7}\text{Zn}_{0.3}\text{Fe}_2\text{O}_4]$, ($0 \leq x \leq 100$ wt%) were prepared using solid state route. Structural and microstructural analysis confirmed the coexistence of ferroelectric (BCZT) and magnetostrictive (NZFO) phases without any detectable presence of impurity/secondary phases. The composites exhibited ferroelectric, magnetic properties and magnetoelectric coupling responses. Highest coupling coefficient was obtained for composite with 50 wt% NZFO.

1. INTRODUCTION

Multiferroics (MFs) are those materials that exhibit, in the same phase (or multiphase), more than one primary ferroic ordering, viz. ferroelectricity, ferro(antiferro/ferri)magnetism, ferroelasticity or ferrotoroidicity [1]. The possibility of coupling between the ferroelectric (FE) and ferromagnetic (FM) order parameters that allows modification of polarization, P (magnetization, M) under an external magnetic field, H (electric field, E) [2], is the most intriguing aspect of MFs.

In this regard, magnetoelectric multiferroic (ME-MF) composites that combine a FE with a FM compound, have been widely studied owing to their superior coupling properties as compared with the single-phase MFs. It is the chemical 'contraindication' between the conventional mechanism of ferroelectricity (requiring empty d -orbitals) and ferromagnetism (facilitated by partially filled d -orbitals), that limits the range of single-phase MFs. Among others, some of the prominent single-phase MF materials are: BiFeO_3 , BiMnO_3 , YMnO_3 , hexagonal manganites RMnO_3 (where R represents a rare earth ion), Fe_3O_4 ,

$\text{Pb}(\text{Fe}_{0.5}\text{Nb}_{0.5})\text{O}_3$ [3]. On the other hand, in ME-MF composites, the ferroelectric phase with large piezoelectric response and the large magnetostrictive coefficient of the magnetic phase allows strain-induced effects between the heterograins of the two phases generating strong ME coupling. Owing to this cross coupling, such composites, when subjected to an external H can tune/switch P (termed as *direct* ME effect; $P_i = \alpha_{ij}^E H_j$, where α_{ij}^E is the linear ME coupling coefficient) and, conversely, M can be modified via an external E (the *converse* ME effect; $\mu_o M_i = \alpha_{ij}^E E_j$, where μ_o is the magnetic permeability of vacuum) [1].

In the *direct* ME effect, the magnetoelectric voltage coefficient which is the voltage (electric field) induced in a sample by an ac magnetic field, is calculated using the relation [4]:

$$\alpha_{ij}^E = \frac{dE_i}{dH_j}$$

From the applications viewpoint, ME MFs can be utilized in novel devices like ultra-low power

high-density logic-memory, micro(nano) electronics, sensors, spintronics, among others [5-7].

In the present study, bulk ME-MF composites with $\text{Ba}_{0.85}\text{Ca}_{0.15}\text{Zr}_{0.1}\text{Ti}_{0.9}\text{O}_3$ (BCZT) as the piezoelectric phase and $(\text{Ni}_{0.7}\text{Zn}_{0.3})\text{Fe}_2\text{O}_4$ (NZFO) as the magnetostrictive phase were prepared and studied for their structural, microstructural and bulk properties (ferroelectric, magnetic, magnetoelectric). In the recent past, BCZT emerged as a promising lead-free compound due to its outstanding piezoelectric coefficient $d_{33} \sim 600$ pC/N [8], rendering BCZT as a favourable candidate for the piezoelectric phase in ME-MF composites. For the magnetostrictive phase, the spinel ferrite, NiFe_2O_4 (NFO), having large magnetostriction coefficient is among the most desired ferromagnetic materials. Literature survey on the relevant topic yielded no reports on composites of BCZT with the $\text{Ni}_{0.7}\text{Zn}_{0.3}\text{Fe}_2\text{O}_4$ composition and was therefore studied.

2. EXPERIMENTAL METHODS

Bulk composites of $(1-x)\text{Ba}_{0.85}\text{Ca}_{0.15}\text{Zr}_{0.1}\text{Ti}_{0.9}\text{O}_3 - x\text{Ni}_{0.7}\text{Zn}_{0.3}\text{Fe}_2\text{O}_4$ [BCZT- x NZFO; $x=0, 10, 30, 50, 70, 90, 100$ wt% or $x=0, 0.1, 0.3, 0.5, 0.7, 0.9, 1$] were fabricated using solid-state reaction method and the details can be found in ref [9]. X-ray diffraction (XRD) and field emission scanning electron microscope (FESEM) equipped with EDS (electron x-ray diffraction spectroscopy) were utilized for structural and microstructural studies. The electric field induced polarization (P - E) loops were acquired on a tracer based on Sawyer-Tower circuit. Magnetic measurements were performed using a vibrating sample magnetometer (VSM Lakeshore model 142A). The ME coupling coefficients were estimated from the magnetically induced voltage.

3. RESULTS AND DISCUSSIONS

The x-ray diffractograms of the powder samples of the sintered composites showed well-defined peaks corresponding to the perovskite BCZT phase and the spinel NZFO phase with no

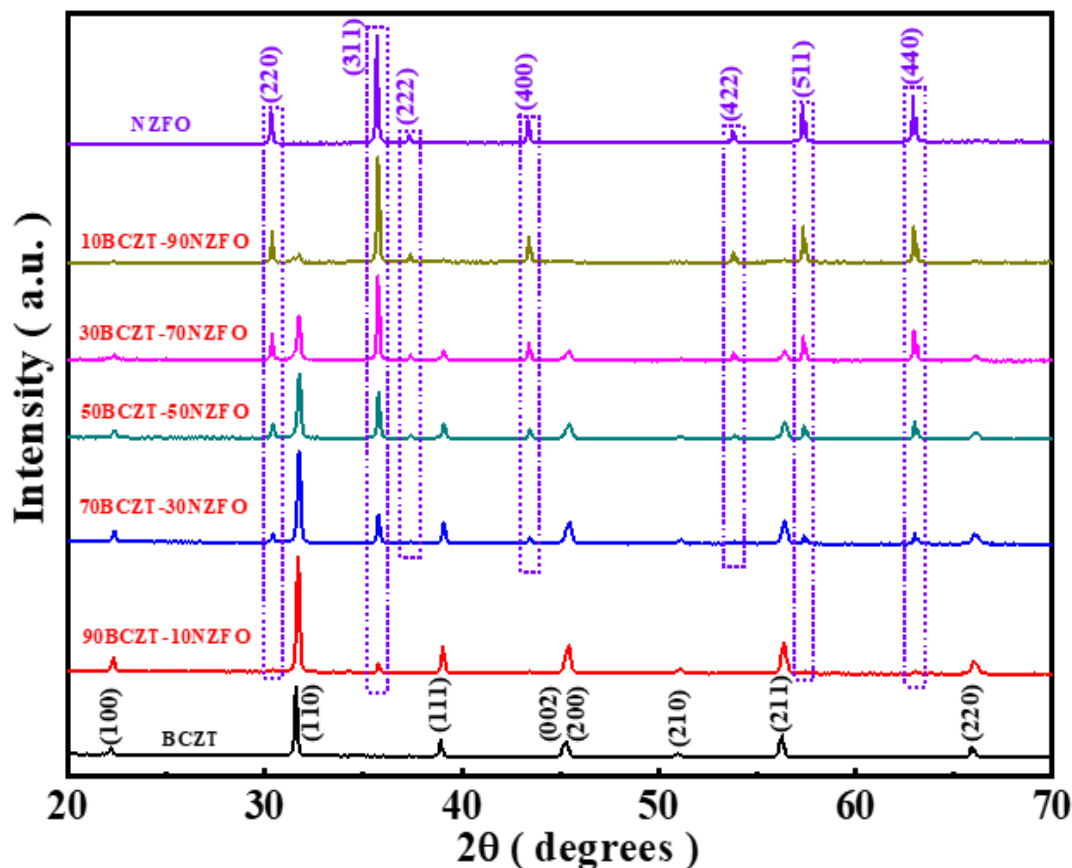


Figure 1. XRD profiles of the BCZT- x NZFO composites.

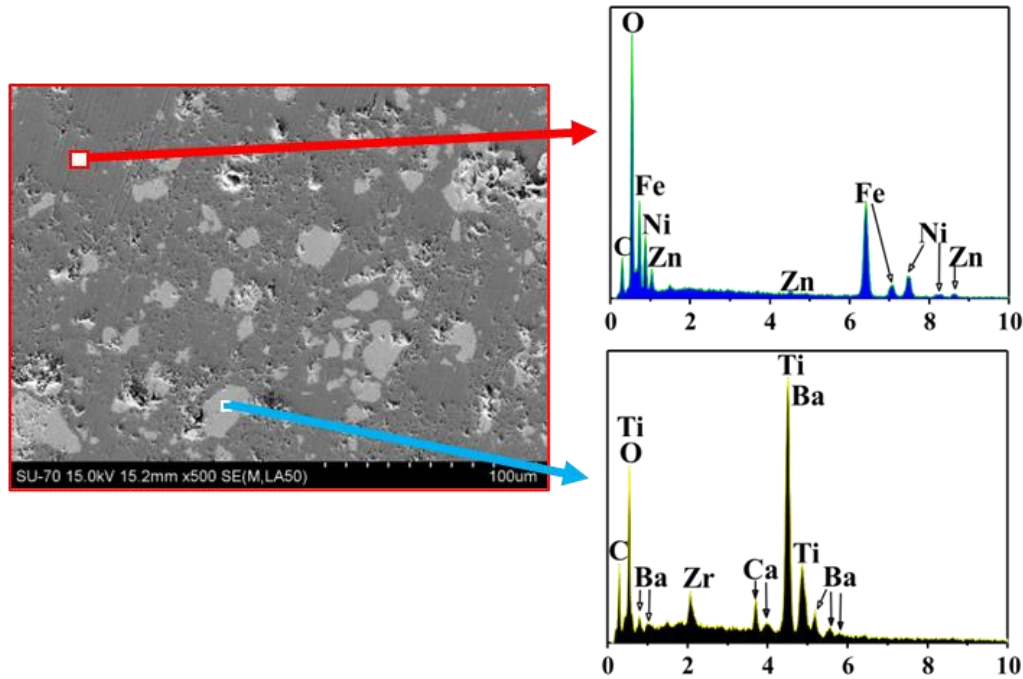


Figure 2. Backscattered electron (BSE) and EDS spectra of 50BCZT-50NZFO composite.

detectable secondary phase (Figure 1). It is observed that the peak intensity of the ferrite phase enhances with increasing content of NZFO (demarcated by dotted boxes) while those of the ferroelectric phase decrease. The density of the composites decreased from ~ 5.3 g/cc to 4.8 g/cc with the addition of the ferrite phase, which is attributed to the lower density of NZFO than BCZT.

The backscattered electron image of a representative sample (50BCZT-50NZFO) is shown in Fig. 2, where the lighter grains correspond to the BCZT while the darker grains

belong to the NZFO phase, respectively, corroborated by the EDS spectrum shown in Fig. 2.

The polarization versus electric field (P - E) hysteresis loops confirmed the ferroelectric nature of the composites (Fig. 3). The saturation polarization was highest in BCZT that decreased with increasing non-ferroelectric ferrite content in the composites. The magnetization response (M - H) exhibited extremely slim, well-saturated hysteresis loops with very small coercivity values suggesting a long-range ferrimagnetic ordering and soft magnetic behaviour (Figure 4). The parameters from M - H loops: coercive field (H_c),

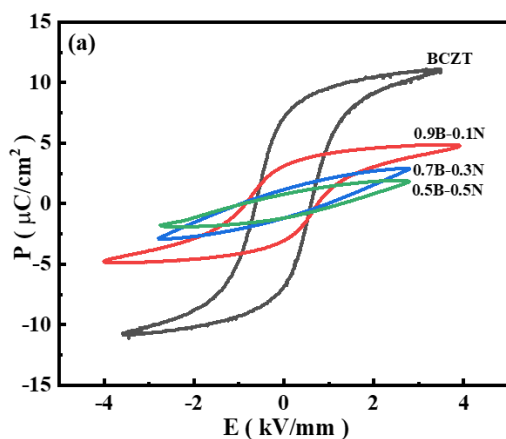


Figure 3. P - E hysteresis loops.

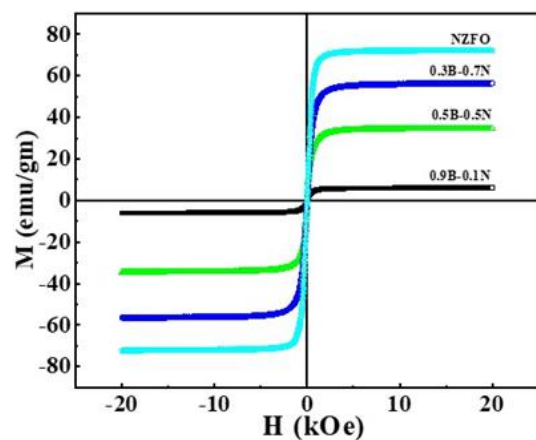


Figure 4. M - H hysteresis loops.

Table 1: M_s , M_r and H_c for the composites

Composition	M_s (emu/g)	M_r (emu/g)	H_c (Oe)
0.9B-0.1N	6.07	0.385	19.2
0.7B-0.3N	23.29	0.521	6.0
0.5B-0.5N	34.6	0.39	3.0
0.3B-0.7N	56.39	1.32	14.0
NZFO	72.36	2.5	20.5

saturation magnetization (M_s), and remanent magnetization (M_r), are enlisted in Table 1. As expected, the presence of the nonmagnetic BCZT phase affects the distribution of the magnetic ions and their spin orientation, and consequently a decrease in M_s and M_r is observed with increasing BCZT content in the composites. The bulk polarization and magnetization studies, thus confirm the co-existence of the individual ferroelectric and magnetic phases in the prepared composites.

In order to attest the coupling between magnetic and electric order parameters, the magnetically induced voltage (ME voltage) was measured by subjecting the samples to an *ac* magnetic field (1 Oe) at 1 kHz in the presence of a *dc* bias magnetic field, H . The ME coupling measurements were performed in two modes: transverse (α_{E31}) and longitudinal (α_{E33}). The coupling coefficient

induced by the varying magnetic field was estimated from the relation: $\alpha_E = \partial E / \partial H \approx \frac{\delta V}{(t \delta H)}$, where δV denotes the voltage measured across the sample having thickness t . Figure 5 compares the ME coupling coefficient in 50BCZT-50NZFO composition which showed the highest $\alpha_{31} \sim 14.5$ mV/Oe.cm and $\alpha_{33} \sim 12.9$ mV/Oe.cm, among the studied composites. It is seen that in both the modes, the α_E trace similar magnetic field dependence: initial increase with magnetic field; thereafter reaching a maximum before gradually decreasing to nearly zero. The α_E curves should follow the piezomagnetic coefficient $q_{ik} (= \frac{d\lambda_{ik}}{dH}$, where λ_{ik} is the magnetostriction) of the magnetic phase as it changes with H . Initially, at lower H , the λ_{ik} is small and thus weak ME response is observed. However, with increasing H , alignment of magnetic moments along the field direction

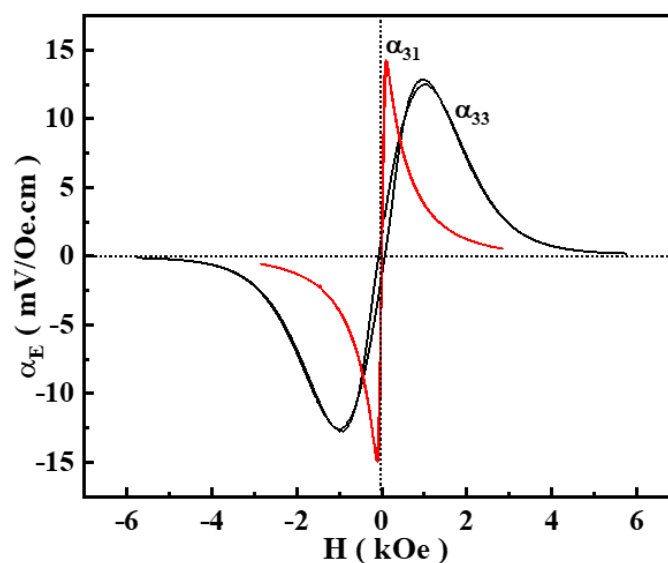


Figure 5. ME coupling coefficient in 50BCZT-50NZFO.

results in an increase in λ , thereby increasing α_E . Whereas at higher fields, λ_{ik} saturates and the piezomagnetic coefficient becomes independent of H and therefore α_E gradually decreases. As also noted, the transverse coupling coefficient is greater than the longitudinal coefficient, although the difference is small. This can be understood on the basis of the phase-field modelling and simulations as explained by Ma *et al.* [10]. Following their report, it is believed that in the present case, electric field poling along 3-axis causes elongation of the piezoelectric phase in the same direction (provided $d_{33} > 0$), which in turn, because of the strain-mediated elastic interaction, produces a strain in the magnetostrictive particulates along the 3-axis. This creates a magnetic domain structure having some extent of magnetization alignment along the ± 3 axis, *i.e.* with a predominant 180 domain wall formation before the application of H . Thus, the bias magnetic field applied along 3-axis in the longitudinal mode mostly drives the 180-domain wall motion. Consequently, there is a small magnetostriction strain leading to smaller coupling coefficient (α_{33}). On the contrary, when H is applied in transverse geometry, a larger change in magnetostriction strain could be obtained *via* non-180-domain wall motion, resulting in higher value of α_{31} .

4. CONCLUSIONS

In conclusion, ME MF composites of (1-x)BCZT – xNZFO were successfully synthesized. The composites exhibited their individual ferroic (ferroelectric and magnetic) characteristics. Maximum ME coupling was achieved in the composite with an optimum weight fraction of 50 wt% ferrite content.

ACKNOWLEDGMENTS

I.C. would like to acknowledge financial assistance by national funds (OE), through FCT – Fundação para a Ciência e a Tecnologia, I.P., in the scope of the framework contract foreseen in the numbers 4, 5 and 6 of the article 23, of the Decree-Law 57/2016, of August 29, changed by Law 57/2017, of July 19. This work was partially developed within the scope of the project CICECO-Aveiro Institute of Materials, UIDB/50011/2020, UIDP/50011/2020 & LA/P/0006/2020, financed by national funds through the FCT/MEC (PIDDAC).

REFERENCES

- [1] N.A. Spaldin and R. Ramesh, *Nat. Mater.* **18(3)**, 203-212 (2019).
- [2] M.I. Bichurin, Magnetolectric Composites. Jenny Stanford Publishing (2019).
- [3] C.A.F.Vaz, J.Hoffman, C.H.Ahn, Ramamoorthy Ramesh, *Advanced Materials* **22(26-27)**, 2900-2918 (2010).
- [4] M.Etier, V.V. Shvartsman, S.Salamon, Y.Gao, H. Wende, D.C.Lupascu, *Journal of the American Ceramic Society* **99(11)**, 3623-3631 (2016).
- [5] S. Manipatruni, D. E Nikonov, Chia-Ching Lin, T. A. Gosavi, H. Liu, B. Prasad, Y.-L.Huang, E. Bonturim, R. Ramesh, I.A.Young, *Nature* **565(7737)**, 35-42 (2019).
- [6] D.K.Pradhan, A.K.Mishra, S.Kumari, A.Basu, M.Somayazulu, E.Graduskaite, R.M. Smith, J. Gardner, P. W. Turner, A. T. N'Diaye, M. B. Holcomb, R. S. Katiyar, P.Zhou, G.Srinivasan, J. M. Gregg & J. F. Scott, *Scientific Reports* **9(1)**, 1685 (2019).
- [7] S. Kumari, *et al.*, B.D. Stojanovic, Editor. 2018, Elsevier. p. 571-591.
- [8] W. Liu, and X. Ren, *Physical Review Letters* **103(25)**, 257602 (2009).
- [9] I. Coondoo, J. Vidal, I. Bdikin, R. Surmenev, A. L. Kholkin, *Ceram. Int.* **48**, 24439 (2022).
- [10] F. D. Ma, Y. M. Jin, Y. U. Wang, S. L. Kampe, S. Dong, *Applied Physics Letters*, **104(11)**, 112903 (2014).

Tunnel magnetoresistance of granular superparamagnetic and ferrimagnetic structures

Gunnar Suchanek

Institute of Solid-State Electronics, TU Dresden, 01062 Dresden, Germany
Corresponding author, e-mail address: Suchanek@tu-dresden.de

Received 1 September 2022; accepted 16 November 2022; published online 20 December 2022

ABSTRACT

Applicable magnetic sensors based on nanogranular ferromagnetic materials were developed already more than 25 years ago. Since the then, nanotechnology has advanced significantly. New methods for manufacturing agglomerated core-shell structures have emerged. This opens up new possibilities of sensor fabrication and an opportunity for reassessment of the electric and magnetic properties of ideal granular structures. This work represents a comprehensive study of the intergranular resistivity, tunnel magnetoresistance and magnetic field sensibility of superparamagnetic and ferro(ferri)magnetic granular materials. Starting with the tunnel resistance of a granular metal network in which the grains are interconnected by insulating barriers, the tunnel magnetoresistance is calculated under consideration of the temperatures dependencies of magnetization, spin polarization and the magnetic flux dependencies of magnetization and tunnelling barrier height. Granular, superparamagnetic materials show a higher magnetic field sensitivity than ferromagnetic ones. They show a lower temperature coefficient of the tunnel magnetoresistance. Owing to their small magnetic response a higher temperature, superparamagnetic ferrimagnetic oxides are not suitable for application at room temperature. Ferromagnetic nanoparticles possess a high field sensitivity only in a small region of 0.1 to 0.5 T.

1. INTRODUCTION

A granular material is a conglomeration of solid particles characterized by a loss of energy whenever the particles interact [1]. A small negative magnetoresistance was observed in granular superparamagnetic (SPM) Ni-SiO₂ thin films of 5-6 nm diameter made by co-sputtering of Ni and SiO₂ already 50 years ago [2]. The appearing magnetoresistance was attributed to tunnelling of spin-polarized electrons between the metallic granules. Its low value is explained by a low spin polarization of Ni amounting to 11 % at low temperatures [3]. Nanogranular, magnetic Fe-B-N thin films were first prepared by cosputtering of Fe-B and BN in 1985 [4]. The films were composed of two amorphous phases of Fe-B and B-N with a size of about 5 nm. They possessed a high specific electrical resistivity ρ in the order of 1-100 m Ω ·cm

and a saturation magnetization of 2.1 μ_B /at at low temperatures. In 1994, large tunnel magnetoresistance (TMR) of 8 % at 1.2 T and room temperature was obtained in Co-Al-O nanogranular films with a resistivity of about 100 m Ω ·cm [5]. These films consist of two phases – SPM, metallic Co granular grains and Al₂O₃ narrow intergrains. Hence, the electrical conductance is governed by tunnelling between Co grains through Al₂O₃ tunnel barriers. Comparable values were reported in the next years for granular Co-Si-O [6], Co-Re-O, Re = Y, Nd, Sm, Gd, Tb, Dy [7], Fe-Al-O [8,9], Fe-Mg-O [10], Fe-Si-O [11,12,13], Fe-Hf-O [14], and Fe-Re-O, Re = Y, Nd, Sm, Gd, Tb, Dy [7]. A TMR of up to 7.5 % at 78 K and 1 T was obtained for granular Fe-MgF₂ thin films [15]. Later in 2001, TMR values up to about 14 % at room temperature and 1 T were observed in a 32 vol%(Fe_{0.51}Co_{0.49})-(Mg-F) thin film [16].

Here, the (Mg-F) intergranules were in the crystalline MgF₂ state enabling a higher TMR compared to Co-Al-O film with an amorphous structure of Al-oxide intergranules. Regardless, the proposed applications of nanogranular magnetic films were just noise suppression in the microwave range [17] and magneto-optic devices based on the Faraday effect [18].

The first granular thin films were mainly fabricated by reactive co-sputtering of two metals or co-sputtering of a metal and a dielectric in a way that a two-phase structure was formed. Since the 2000ies, nanotechnology has advanced significantly. New methods for manufacturing agglomerated core-shell structures have emerged. This opens up new possibilities of sensor fabrication and an opportunity for reassessment of the electric and magnetic properties of ideal granular structures.

In this work, the intergranular resistivity, tunnel magnetoresistance and magnetic field sensibility of SPM and ferro(ferri)magnetic (FM) granular materials are examined theoretically. Starting with the tunnel resistance of a granular metal network in which the grains are interconnected by insulating barriers, the tunnel magnetoresistance is calculated under consideration of the temperatures dependencies of magnetization, spin polarization and the magnetic flux dependencies of magnetization and tunnelling barrier height. Both, SPM and FM nanoparticles (NPs) are considered.

2. INTERGRANULAR RESISTIVITY, TUNNEL MAGNETORESISTANCE AND MAGNETIC FIELD SENSIBILITY

2.1. Intergranular resistivity and magneto-resistance caused by spin-polarized tunnelling

The resistivity of a granular metal network in which the metal grains are interconnected by insulating barriers is given by [19]

$$\rho_T(T) \propto \exp\left(f\chi w + \frac{E_c}{2kT}\right), \quad (1)$$

where f is a barrier shape factor, $f=2$ for rectangular barriers and $f=\pi/2$ for parabolic barriers, χ is the reciprocal localization length of the wave function

$$\chi = \sqrt{\frac{2m^*V_0}{\hbar^2}}, \quad (2)$$

with m^* is the effective electron mass, V_0 the barrier height, \hbar is the reduced Planck constant, w the barrier width, E_c the charging energy of the grains, k the Boltzmann constant, and T the absolute temperature. Note that we are considering thin enough barriers in the order of 1 to 3 nm where direct tunnelling occurs which is not disturbed by localized states in the thin barrier film. An estimation of E_c for grains of diameter d – much larger than the barrier width w – is given by equation [20]

$$E_c \approx \frac{4e^2w}{\varepsilon\varepsilon_0d^2}, \quad (3)$$

with ε the dielectric permittivity and ε_0 the vacuum permittivity, respectively. Since the charging energy is reciprocal to the grain diameter, charging effects become significant at small grain sizes.

Tunnelling itself is a temperature-independent transport process [21]. Spin-dependent electron tunnelling depends on the relative orientation of magnetic moments between the ferrimagnetic grains. The tunnel resistance decreases when the magnetic moments of the grains are aligned in parallel in an applied magnetic field. If the angle between the magnetizations on both sides of the tunnelling barrier is randomly distributed between 0 and π , the resistivity given by [22]

$$\rho_T(T) = \frac{\rho_0 \cdot \exp(f\chi w)}{1 + m^2(B, T) \cdot P^2}, \quad (4)$$

with m the relative magnetization, i.e. the magnetization scaled to the saturation magnetization, and P the spin polarization in the magnetic grains.

The temperature dependence of the tunnelling spin polarization can be represented as follows [23]

$$P(T) = P_0(1 - g_P T^{3/2}), \quad (5)$$

where P_0 equals to 0.44, 0.34, 0.85, 0.72 and 0.55 for Fe, Co, La_{2/3}Sr_{1/3}MnO₃, Sr₂FeMoO_{6- δ} and Fe₃O₄ respectively, whereas g_P can be estimated using the Curie temperature T_C

$$g_P \approx T_C^{-3/2}. \quad (6)$$

Following equation (2), the decay of wavefunction in a barrier material depends on the barrier height. Consequently, we have to consider the barrier height in dependence on the magnetic flux density B . The magnetic field dependence of the tunnelling barrier was taken in the form of a series expansion [24]

$$V_0(B) = V_0(0) - \beta B + \gamma B^2. \quad (7)$$

The coefficient β is attributed in to Zeeman splitting amounting about $1 \mu_B$, i.e., 0.058 meV/T for a magnetic field perpendicular and about $20 \mu_B$ for a magnetic field applied parallel to the current. The coefficient γ is adapted from data of a magnetic sensor based on a tunnelling device comprising a 2 nm thick double perovskite $\text{La}_2\text{Co}_{0.8}\text{Mn}_{1.2}\text{O}_6$ layer grown on top of a Nd-doped SrTiO_3 substrate and capped with a thin Pt layer [24].

We have developed a more complex model for the intergranular TMR of strontium ferromolybdate ($\text{Sr}_2\text{FeMoO}_{6-\delta}$, SFMO) ceramics caused by spin-polarized tunnelling [25]. Taking the resistivity of a granular metal network in which the metal grains are interconnected by insulating barriers, equation (1), and accounting only small changes of the barrier height by the applied magnetic field, this yields a TMR of

$$TMR = \frac{\rho(B)}{\rho(0)} - 1 = \frac{(1+m(0,T)^2 \cdot P^2) \cdot \exp\left(f\chi(0) \cdot w \cdot \frac{\delta V_0}{2V_0}\right)}{(1+m(B,T)^2 \cdot P^2)} - 1, \quad (8)$$

where $\rho(B)$ is the resistivity for a given magnetic flux density B . For very large barrier heights and very soft magnetic materials we obtain the well-known relation [26]

$$TMR = -\frac{m^2 P^2}{1+m^2 P^2} = \frac{1}{1+m^2 P^2} - 1. \quad (9)$$

In the latter model, the maximum TMR is -50 %.

2.2. Granular networks of noninteracting superparamagnetic nanoparticles

The remanent magnetization of uniaxial, single-domain NPs which are fully magnetized along the easy axis vanishes after removing the magnetic field as

$$M = M_s \exp\left(-\frac{t}{\tau}\right), \quad (10)$$

where M_s is the saturation magnetization, t the time after removal of the field. The value τ denotes the Néel-Brown relaxation time for an energy barrier $\Delta E = KV$ [27,28]

$$\tau = \tau_0 \exp\left(\frac{KV}{kT}\right), \quad (11)$$

with τ_0 a time constant in the order of nanoseconds [29], K the uniaxial anisotropy constant, V the particle volume. Note that the uniaxial anisotropy constant is also temperature dependent [30].

SPM behavior is obtained using an instrument with a characteristic measuring time τ_m larger than τ . For τ_m less than τ , the magnetic moments remain in a fixed direction during the measurement. This leads to a remanent magnetization and appearance of a coercive field, thus, a metastable FM state is detected. The condition $\tau = \tau_m$ defines the so-called blocking temperature T_B [31]

$$T_B = \frac{KV}{k \cdot \ln(\tau_m / \tau_0)}. \quad (12)$$

Here, the characteristic measuring time amounts to ca. 100 seconds in static magnetometry [32]. Particles above the blocking temperature reveal a dominating SPM behaviour, while particles below the blocking temperature show a predominant FM behaviour. In the latter case thermal excitations are not sufficient to overcome the energetic barrier. The critical size below which SPM behaviour is obtained, d_{cr}^{spm} , then yields

$$d_{cr}^{spm} = \left(\frac{\pi \cdot \ln(\tau_m / \tau_0) \cdot kT}{6 \cdot K(T)}\right)^{1/3}. \quad (13)$$

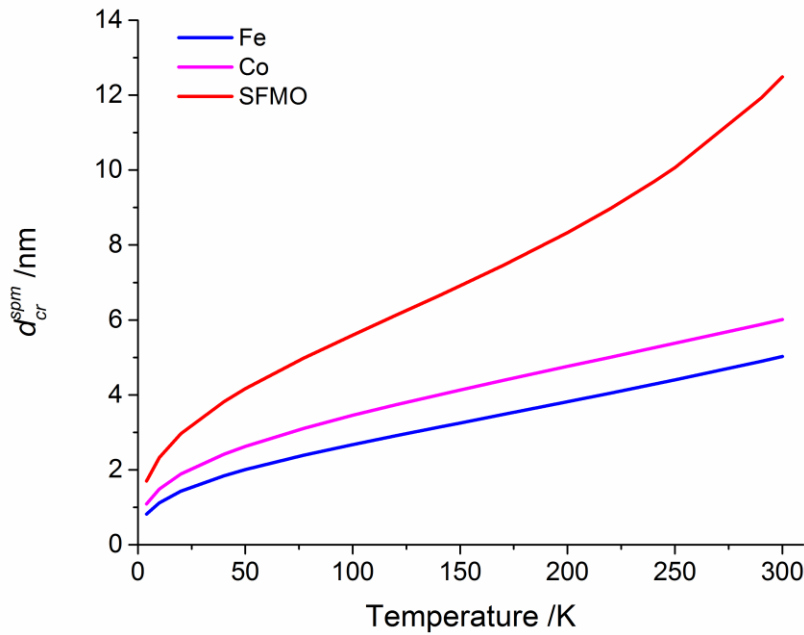


Figure 1. Temperature dependence of the SPM critical diameter, equation (13).

Figure 1 shows the temperature dependence of the critical size of Fe, Co and SFMO.

$K(T)$ varies as a function of the reduced temperature T/T_C with T_C the Curie temperature

$$K(T) = K(0) \cdot \left(1 - \frac{T}{T_C}\right)^\eta. \quad (14)$$

On the other hand, the dependence of the anisotropic constant on magnetization obeys a power law

$$\frac{K(T)}{K(0)} = \left[\frac{M(T)}{M(0)}\right]^n, \quad (15)$$

with a coefficient $n = 3$ for uniaxial anisotropy and $n = 10$ for cubic one [33,34]. In the presentation of equation (15), the reduced magnetization has a power coefficient of $1/3$

$$m = \frac{M_s(T)}{M_s(0)} = \left(1 - \frac{T}{T_C}\right)^{1/3}, \quad (16)$$

which was derived from Monte-Carlo and Landau–Lifshitz–Gilbert simulations [35]. This yields $\eta = 10/3$ and $\eta = 1$ for SFMO. The experimental value of η for core-shell $\text{Sr}_2\text{FeMoO}_{6-\delta}$ - SrMoO_4 core-shell structures amounts to $\eta = 4/3$ [36]. At

nonideal interfaces, the second-order anisotropy constant comes into play [37] so that in our case the power coefficient becomes $\eta > 1$. A value of $n = 4$ indicates that the second-order anisotropy constant plays a significant, albeit not overwhelming, role.

With regard that the approximations made for the reduced magnetization fail at very low temperatures, we have to deal with particles sizes in the order of 5 to 10 nm. Reducing further the NP size, surface effects become dominant and the ideal model of a giant spin formed by all the spins of the particle pointing in the anisotropy direction and coherently reversing due to thermal activation is no longer valid. For example, fcc Co NPs having about 200 atoms will have diameters around 1.6 nm and 60% of the total spins are located at the surface [38]. Surface spin canting reduces the magnetization yielding strong deviations from the bulk behaviour. This latter size effect is beyond the scope of this paper.

The reduced magnetization of SPM NPs resembles the Langevin behavior of paramagnetic materials [32]

$$m = \frac{M_s(T)}{M_s(0)} = L(\zeta B) = \frac{\coth(\zeta B) - 1/(\zeta B)}{\zeta}, \quad \zeta = \frac{\mu}{kT}, \quad (17)$$

where μ is the magnetic moment of the NP depending on its size. Note that Eq. (17) is valid only for a noninteracting system [2]. The effects of interactions may be accounted for by adding a mean field to the applied field, i.e., $B=B_a+\mu_0\lambda M$ with B_a the applied magnetic flux and λ an interaction parameter. Figure 2 shows the reduced

magnetization of iron NPs with a diameter of 10 nm with the magnetic flux density as a parameter. Note that SPM particles above T_B show no hysteresis. However, since the SPM NP acts as a giant spin, the magnetization and the magnetic susceptibility of a SPM material are much larger compared to that of a paramagnetic material.

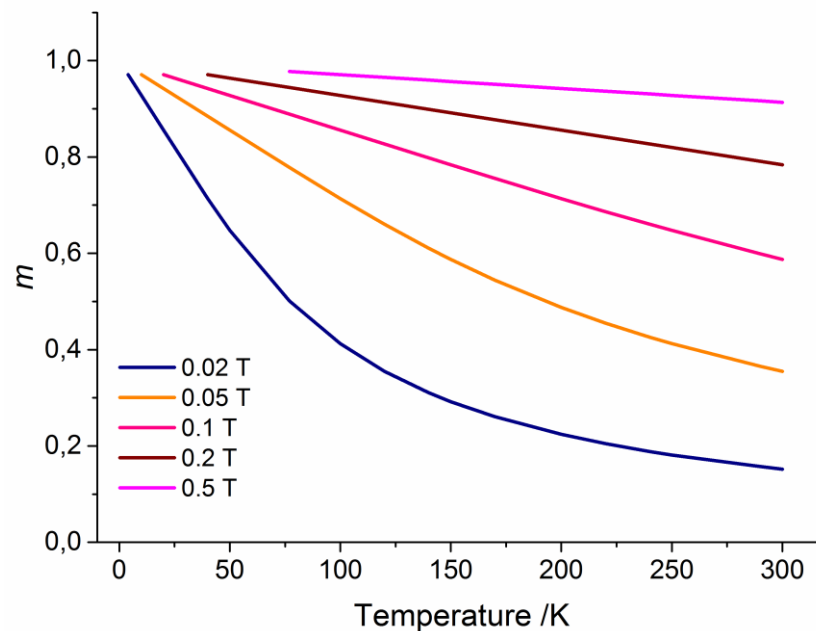


Figure 2. Temperature dependence of the reduced magnetization of Fe NPs with a $d = 10$ nm.

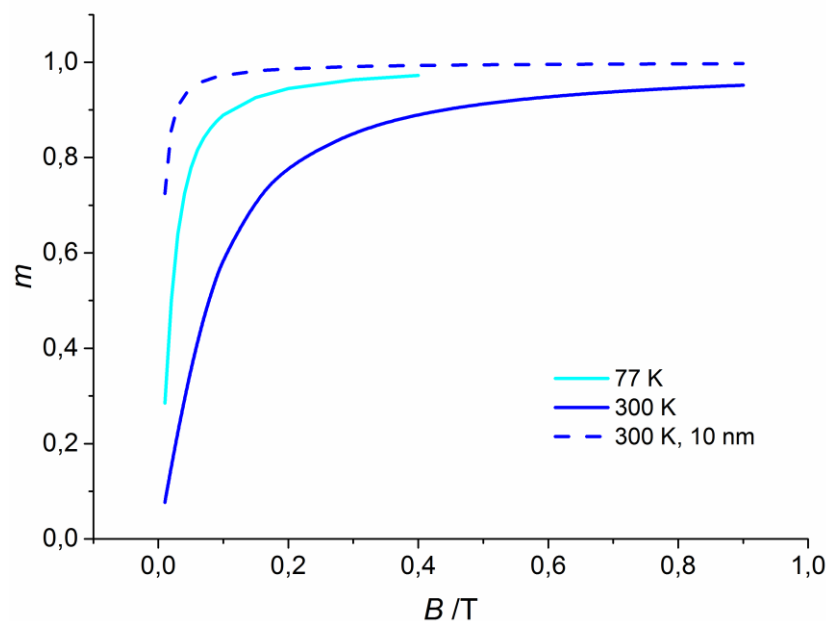


Figure 3. Magnetic flux dependence of the reduced magnetization of Fe NPs with a $d = 4$ nm. The curve for $d = 10$ nm at 300 K is shown for comparison.

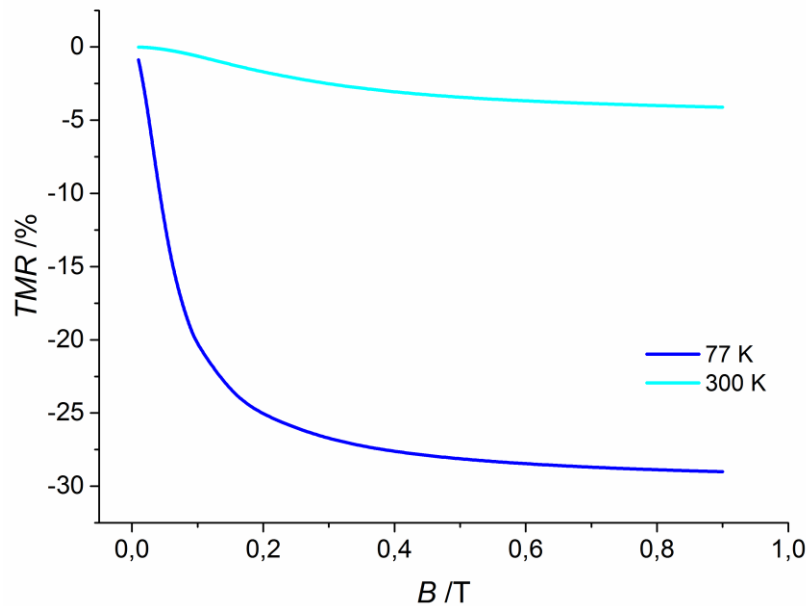


Figure 4. Magnetic flux dependence of the TMR of SPM SFMO NPs with $d = 10$ nm.

Figure 3 depicts the field dependence of NPs with a diameter of 4 nm. Liquid nitrogen is suitable as a coolant for magnetic sensors to provide the condition of a constant temperature and to avoid thermal fluctuations. For this reason, data calculated for 77 K is shown in the following for comparison.

Figure 4 illustrates the TMR for SPM SFMO NPs of about 10 nm diameter calculated by means of equations (5), (9) and (17). Here, a temperature dependence appears due to the temperature dependencies of spin polarization and magnetization. The temperature coefficient of the TMR (TC_{TMR}) amounts to $-8.7 \cdot 10^{-3}$ and $-2.1 \cdot 10^{-2} \text{ K}^{-1}$ at 0.1 T and 77 and 300 K, respectively. SPM SFMO NPs are suitable for application as a magnetic field sensor at liquid nitrogen temperatures in the magnetic field range up to about 100 mT.

Now we turn to a special tunnelling effect in granular systems at low temperatures. We start with the resistance in granular systems – equation (1) – and the corresponding TMT – equation (9). In the granular systems with a broad distribution in granule size, it is highly probable that large granules are well separated from each other due to their low number density (that is, the larger the granule size is, the more separated the granules are). As a result, a number of smaller granules exist separating the large ones. Here, the ordinary

tunnelling of an electron from the large granule to the small one increases the charging energy E_c , cf. equation (3), and suppresses tunnelling by the Coulomb blockade at low temperatures. In this case, higher-order tunnelling comes into play, i.e., the dominant contribution to the tunnelling current now comes from higher-order processes of spin-dependent tunnelling where the carrier is transferred from the charged large granule to the neighbouring neutral large granule through an array of small granules, using co-tunnelling of $(p+1)$ electrons. The TMR is then given by [39]

$$TMR = \frac{1}{(1 + m^2 P^2)^{1+p^*}} - 1, \quad p^* = \frac{p^*(0)}{\sqrt{T}}, \quad (18)$$

where $p^*(0)$ is a fitting parameter $p^*(0) > 2$ which is determined by the maximum of the distribution of conduction paths $f(p)$.

Figure 5 shows the calculated TMR of Co NPs due to higher order tunnelling – equation (18) – compared with the TMR without higher order tunnelling – equations (5) (9) and (17) – and experimental data attributed to higher order tunnelling in granular Co- Al_2O_3 [40]. Similar effects occur in granular zinc ferrite-ferric oxide [41]. High order tunnelling does not occur at room temperature since here p^* tends to zero.

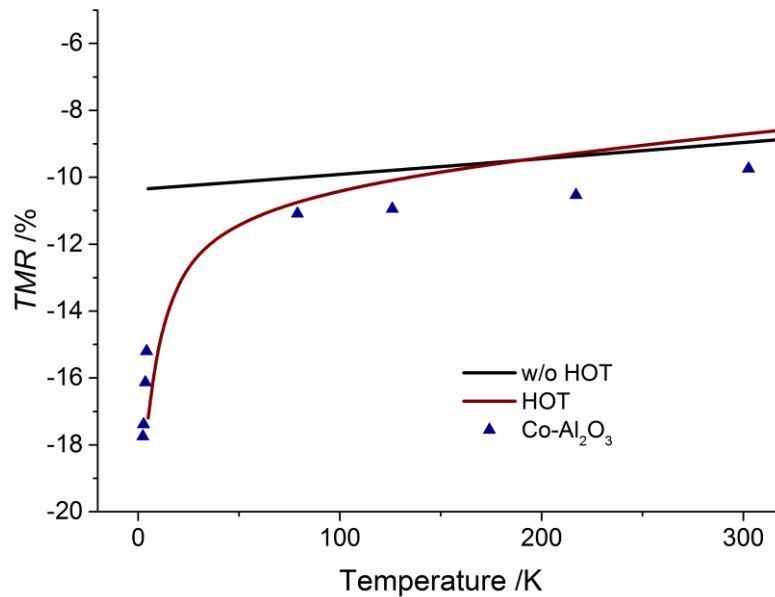


Figure 5. Calculated TMR of Co NPs due to higher order tunnelling compared with the TMR without higher order tunnelling and experimental data of granular Co with $d = 2\text{-}3$ nm interconnected by a 1 nm thick Al_2O_3 barrier [40].

The magnetic field sensibility of a sensor is the derivative of the sensor signal by the magnetic flux density. When interparticle interactions are non-negligible, the magnetic behaviour becomes more complicated requiring a more complex theoretical treatment. Moreover, the interaction energy depends on the particular arrangement (volume, topology) of the NPs. On the other hand, the NPs of granular network are interconnected by insulating barriers. In this case, exchange interaction between spherical particles is negligible and only the magnetic-dipole interaction is significant. For sake of simplicity, we consider NPs as a magnetic dipole in its centre. Then adjacent particles influence each other via their dipolar coupling. Strong interactions will cause agglomerations of SPM NPs leading to hysteretic behaviour. Following the $1/r^3$ -decay of the dipole field, the cut-off radius of dipolar interaction amounts to about five times the average SPM NP radius [42]. Spin dependent tunnelling occurs through thin enough barriers – in the order of 1 to 3 nm – where direct tunnelling occurs which is not disturbed by localized states in the thin barrier film. Here, magnetic coupling increases the stiffness magnetic behaviour lowering the response to an external magnetic field.

Early theoretical models of weak coupling in the presence of an interaction field in spin-glasses [43] and of dipolar interaction of two magnetic particles taking into account uniaxial magnetic anisotropy [44] predicted a decrease of T_B – equation (12) – with increasing magnetic interaction. Contrarily, Monte Carlo simulations studying dipolar interaction and polydispersity of single-domain ultrafine FM particles revealed an increase of T_B with increasing strength of interaction [45]. However, due to the onset of ordering at temperatures in the order of T_B , changes of T_B obtained magnetization measurements will be small. Thus, an upper limit of the magnetic field sensibility was calculated considering noninteracting SPM NPs. This yields

$$\frac{d(\text{TMR})}{dB} = -\frac{2P^2L'(\zeta B)}{[1+P^2L(\zeta B)^2]^2} = -\frac{2P^2\zeta \cdot \left[\frac{1}{(\zeta B)^2} - \frac{1}{\sinh^2(\zeta B)} \right]}{\left\{ 1+P^2 \left[\coth(\zeta B) - \frac{1}{\zeta B} \right]^2 \right\}^2}, \quad (19)$$

where $L(\zeta B)$ is the Langevin function given in equation (17).

Figure 6 illustrates the magnetic field sensibility of noninteracting, SPM Co NPs calculated using equation (5) and (17). A constant value is obtained

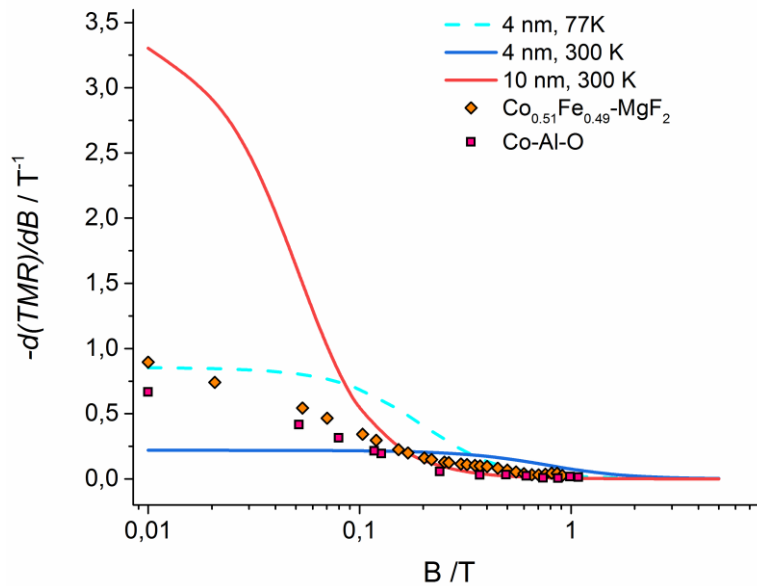


Figure 6. Upper limit of the magnetic field sensitivity of the TMR of SPM Co NPs with a diameter of 4 nm at 77 and 300 K and 10 nm at 300 K, respectively, compared with the field sensitivity derived from experimental data values of Co-Al-O [5] and Co_{0.51}Fe_{0.49}-MgF₂ [46] at 300K.

at low fields of practical interest. TC_{TMR} value without higher order tunnelling is about $-2.14 \cdot 10^{-4} \text{ K}^{-1}$ at low temperatures while it increases to about $-3 \cdot 10^{-2} \text{ K}^{-1}$ at 4 K with higher order tunnelling (cf. Figure 5). Note that cooled to 77 K sensors possess a higher sensitivity.

2.3. Granular networks of ferromagnetic nanoparticles

Up to now, there is no satisfactory analytical expression for the relative magnetization $m(T)$, i.e. the spontaneous magnetization M scaled to the saturation magnetization M_s at low temperatures, except for the two limiting cases, small temperatures $T \rightarrow 0$ and temperatures when approaching the Curie temperature $T \rightarrow T_C$ [47]. For sake of simplification, we make use of the simulation of the temperature dependent magnetization by Monte Carlo methods and

Landau–Lifshitz–Gilbert atomistic spin models, equation (16) [35]. To calculate the temperature dependence of the reduced magnetization, we have used an approximation of m^2 known for Ni near Curie temperature [48] and made a series expansion [25]

$$m^2(T) = \sum_i a_i \left(1 - \frac{T}{T_C}\right)^i, \tag{20}$$

The magnetic flux density dependence of the reduced magnetization was modelled by means of a traditional analysis of the approach of magnetization to saturation [49,50]

$$m(B) = 1 - \sum_i \left(\frac{b_{i/2}}{B}\right)^{i/2}, \tag{21}$$

Table 1. Coefficients of the series expansion, equation (20) [25].

Parameter	Value
a_1	2.0
a_2	-2.3
a_3	2.6
a_4	-1.3

Table 2. Coefficients of the series expansion, equation (21) [25].

Parameter	Value, mT
$b_{1/2}$	7.4
b_1	16

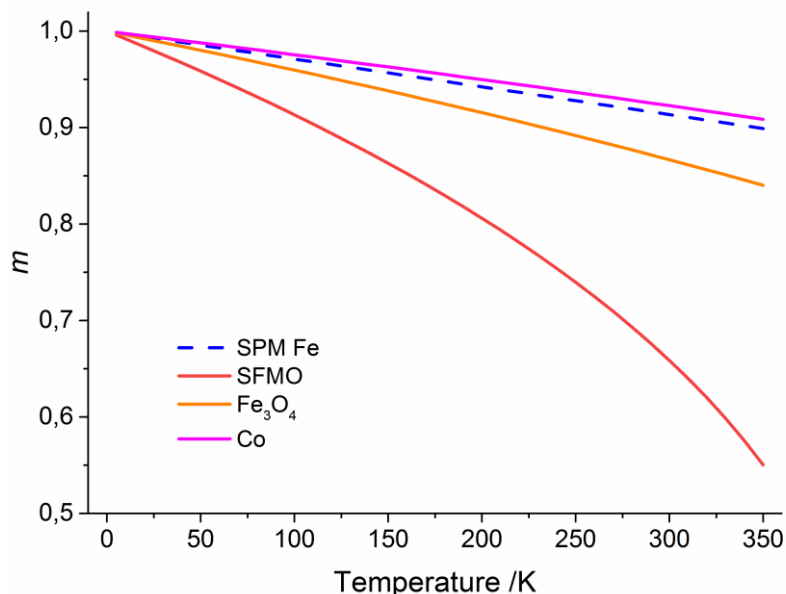


Figure 7. Comparison of the reduced magnetization m of FM SFMO, Fe_3O_4 and Co, equation (16), compared to the values of SPM Fe NPs with $d = 10$ nm at $B = 0.5$ T, equation (17).

Here, each of the lower terms of this expansion is associated with a certain source of magnetic inhomogeneities. i equals 1, 2, 3 for point, linear and layered sources, respectively [50]. On the other hand, the coefficient $b_{1/2}$ in SFMO ceramics was related also to the spin-glass-like behaviour of grain boundaries, the quadratic terms ($i = 4$) is

related to the magnetocrystalline or shape anisotropy as well as to mechanical stress, the cubic term ($i = 6$) also includes magnetocrystalline anisotropy [25]. The corresponding coefficients for SFMO ceramics are shown in Table 1 and 2.

Figure 7 shows the comparison of reduced magnetization in the and FM and SPM state. In the

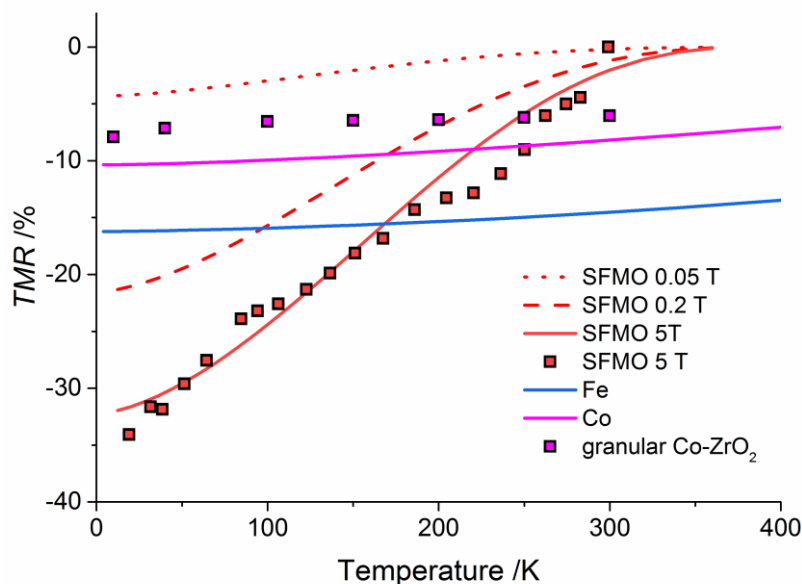


Figure 8. Calculated TMR of granular, ferrimagnetic SFMO in comparison with granular FM Fe, Co and experimental data of granular SPM Co-ZrO₂ thin films [53] as well as nanosized SFMO-SrMoO₄ core-shell structures fabricated by the citrate-gel technique [54].

first case, examples are SFMO, Fe_3O_4 and Co, while in the second case SPM Fe NPs at 0.5 T were considered. High values of the reduced magnetization at room temperature are obtained for high Curie temperatures.

Figure 8 shows the calculated TMR of granular, FM SFMO with the magnetic flux as parameter. The spin polarization at a given temperature was estimated by equation (5) and the reduced saturated magnetization by means of equation (20). Note that at lower magnetic fluxes, the magnetization is lower than the saturated one. For comparison, we consider Fe and Co, where a phenomenological model of the temperature dependence of m [51],

$$m = \left[1 - \left(\frac{T}{T_C} \right)^p \right]^\beta, \quad (22)$$

was applied. The corresponding fitting parameters p and β are compiled in table 3. Also shown is a comparison with experimental data of SPM Co-ZrO₂ granular structures [52].

Due to a small TMR, SFMO is not applicable in magnetic sensors near room temperature. Co and Fe provide suitable values. The temperature

dependence of the TMR of both Fe and Co are weak due to a weak temperature dependence of spin polarization. The TC_{TMR} values of Co and Fe increase with temperature reaching $-6.5 \cdot 10^{-4}$ and $-3.2 \cdot 10^{-4} \text{ K}^{-1}$ at room temperature, respectively.

The magnetic field sensitivity of granular FM materials is given by

$$\frac{d(\text{TMR})}{dB} = - \frac{2P^2 \frac{dm(B)}{dB} \cdot m(B) \cdot m^2(T)}{\left[1 + P^2 m^2(T) \cdot m^2(B) \right]^2}, \quad (23)$$

Figure 9 illustrate the calculation of the magnetic field sensitivity of granular FM Fe, Co and SFMO using equations (5), (21) and (23). Note that the curves in figure 9 depend significantly on the chosen model of m . For instance, the coefficients of SFMO in equation (21) are highly dependent on synthesis condition since they are determined by magnetic inhomogeneities.

Table 3. Parameters of equation (22) [51].

Compound	p	β
Fe	2.876	0.339
Co	2.369	0.34

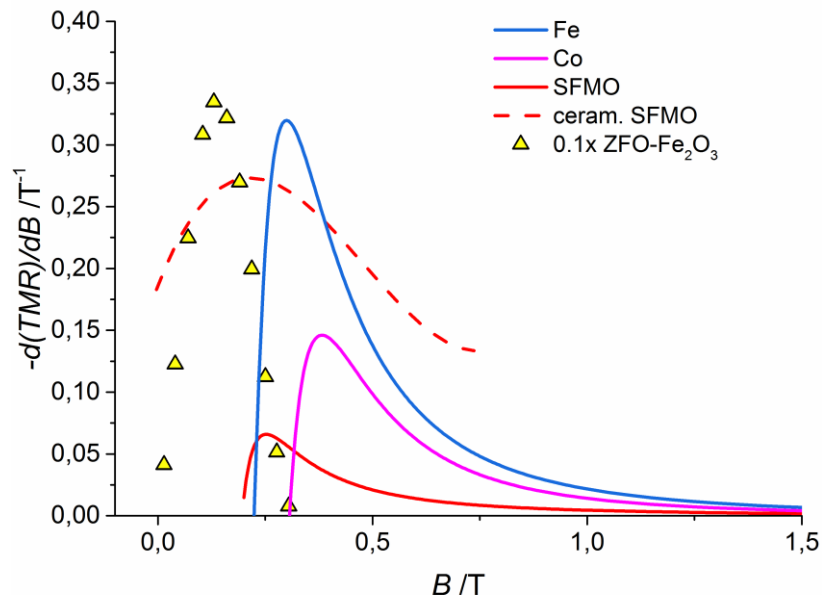


Figure 9. Magnetic field sensitivity of the TMR of FM Fe, Co and SFMO NPs at 300 K, respectively, in comparison with experimental data of ceramic SFMO annealed in reducing atmosphere at 10 K [54] and $\text{Zn}_{0.41}\text{Fe}_{2.59}\text{O}_4$ - α - Fe_2O_3 core shell structure (multiplied by 0.1) with a size of about 160 nm at 300 K [41].

3. CONCLUSIONS

Granular, SPM materials show a higher magnetic field sensitivity than ferromagnetic ones. Also, they show a lower TC_{TMR}. Owing to their small magnetic response a higher temperature, SPM FM oxides are not suitable for application at room temperature. FM nanoparticles possess a high field sensitivity only in a small region of 0.1 to 0.5 T.

ACKNOWLEDGMENTS

This work was developed within the scope of the European project H2020-MSCA-RISE-2017-778308–SPINMULTIFILM.

REFERENCES

- [1] J. Duran, *Sands, Powders, and Grains: An Introduction to the Physics of Granular Materials*, Springer Inc., New York, (1999).
- [2] J. I. Gittleman, Y. Goldstein, and S. Bozowski, *Phys. Rev. B* **5**, 3609 (1972).
- [3] P. M. Tedrow and R. Meservey, *Phys. Rev. B* **7**, 318 (1973).
- [4] H. Karamon, T. Masumoto and Y. Makino, *J. Appl. Phys.* **57**, 3527 (1985).
- [5] H. Fujimori, S. Mitani, and S. Ohnuma, *Mater. Sci. Eng. B* **31**, 219 (1995).
- [6] A. Milner, A. Gerber, B. Groisman, M. Karpovsky, and A. Gladkikh, *Phys. Rev. Lett.* **76**, 475 (1996).
- [7] N. Kobayashi, S. Ohnuma, T. Masumoto, S. Mitani, and H. Fujimori, *J. Magn. Soc. Jpn* **21**, 461 (1997).
- [8] H. Fujimori, S. Mitani, and S. Ohnuma, *J. Magn. Mater.* **156**, 311 (1996).
- [9] Y. H. Huang, J. H. Hsu, and J. W. Chen, *IEEE Trans. Magn.* **33**, 3556 (1997).
- [10] S. Mitani, Y. Shintani, S. Ohnuma, and H. Fujimori, *J. Magn. Soc. Jpn* **21**, 465 (1997).
- [11] S. Honda, T. Okada, and M. Nawate, *J. Magn. Mater.* **165**, 153 (1997).
- [12] S. Honda, T. Okada, M. Nawate, and M. Tokumoto, *Phys. Rev. B* **56**, 14566 (1997).
- [13] B. Zhao and X. Yan, *Physica A* **241**, 367 (1997).
- [14] Y. Hayakawa, N. Hasegawa, A. Makino, S. Mitani, and H. Fujimori, *J. Magn. Mater.* **154**, 175 (1996).
- [15] T. Furubayashi and I. Nakatani, *J. Appl. Phys.* **79**, 6258 (1996).
- [16] N. Kobayashi, S. Ohnuma, T. Masumoto and H. Fujimori, *J. Appl. Phys.* **90**, 4159 (2001).
- [17] S. Ohnuma, M. Ohnuma, H. Fujimori, and T. Masumoto, *J. Magn. Mater.* **310**, 2503 (2007).
- [18] N. Kobayashi, K. Ikeda, Bo Gu, S. Takahashi, H. Masumoto, and S. Maekawa, *Sci. Rep.* **8**, 4978 (2018).
- [19] J. S. Helman and B. Abeles, *Phys. Rev. Lett.* **37**, 1429 (1976).
- [20] B. Abeles, Ping Sheng, M.D. Coutts and Y. Arie, *Adv. Physics* **24**, 407 (1975).
- [21] J. G. Simmons, *J. Appl. Phys.* **34**, 1793 (1963).
- [22] J. Inoue and S. Maekawa, *Phys. Rev. B* **53**, R11927 (1996).
- [23] G. Suchaneck, *Electron. Mater.* **3**, 227 (2022).
- [24] L. López-Mir, C. Frontera, H. Aramberri, K. Bouzeshouane, J. Cisneros-Fernández, B. Bozzo, L. Balcells, and B. Martínez, *Sci. Rep.* **8**, 861 (2018).
- [25] E. Artiukh and G. Suchaneck, *Open Ceram.* **7**, 100171 (2021).
- [26] D. Serrate, J. M. De Teresa, P. A. Algarabel, M. R. Ibarra, and J. Galibert, *Phys. Rev. B* **71**, 104409 (2005).
- [27] L. Néel, *Ann. Geophys.* **5**, 99 (1949).
- [28] W. F. Brown, *Phys. Rev.* **130**, 1677 (1963).
- [29] B. D. Cullity and C.D. Graham, *Introduction to Magnetic Materials*, p. 384, John Wiley & Sons Inc., Hoboken (NJ) (2008).
- [30] C. Zener, *Phys. Rev.* **96**, 1335 (1954).
- [31] C. L. Chien, *J. Appl. Phys.* **69**, 5267(1991).
- [32] C. P. Bean and J. D. Livingston, *J. Appl. Phys.* **30**, S120 (1959).
- [33] E. R. Callen and H. B. Callen, *J. Phys. Chem. Solids* **27**, 1271 (1966).
- [34] S. Chikazumi, *Physics of Ferromagnetism*, 2nd ed., p. 273, Oxford University Press, Oxford, (1997).
- [35] R. F. L. Evans, W. J. Fan, P. Chureemart, T. A. Ostler, M. O. A. Ellis, and R. W. Chantrell, *J. Phys.: Condens. Matter* **26**, 103202 (2014).
- [36] G. Suchaneck, N. Kalanda, M. Yarmolich, E. Artiukh, G. Gerlach and N. A. Sobolev, *Electron. Mater.* **3**, 82 (2022).
- [37] F. Ibrahim, A. Hallal, A. Kalitsov, D. Stewart, B. Dieni, and M. Chshiev, *Phys. Rev. Appl.* **17**, 054041 (2022).
- [38] X. Batlle, A. Labarta, *J. Phys. D: Appl. Phys.* **35**, R15 (2002).
- [39] S. Mitani, S. Takahashi, K. Takanashi, K. Yakushiji, S. Maekawa, and H. Fujimori, *Phys. Rev. Lett.* **81**, 2779 (1998).
- [40] S. Mitani, H. Fujimori, K. Takanashi, K. Yakushiji, J.-G. Ha, S. Takahashi, S. Maekawa, S. Ohnuma, N. Kobayashi, T. Masumoto, M. Ohnuma and K. Hono, *J. Magn. Mater.* **198-199**, 179 (1999).
- [41] P. Chen, D.Y. Xing, Y.W. Du, J. M. Zhu, and D. Feng, *Phys. Rev. Lett.* **87**, 107202 (2001).
- [42] V. Schaller, G. Wahnström, A. Sanz-Velasco, P. Enoksson, P. J. Johansson, *J. Magn. Mater.* **321**, 1400 (2009).
- [43] S. Shtrikman and E. P. Wohlfarth, *Phys. Lett. A* **85**, 467 (1981).
- [44] J L Dormann, L Bessais and D Fiorani, *J. Phys. C: Solid State Phys.* **21**, 2015 (1988).
- [45] J. García-Otero, M. Porto, J. Rivas, and A. Bunde, *Phys. Rev. Lett.* **84**, 167 (2000).
- [46] N. Kobayashi, S. Ohnuma, T. Masumoto and H. Fujimori, *J. Appl. Phys.* **90**, 4159 (2001).
- [47] G. Suchaneck, *Mod. Electron. Mater.* **7**, 85 (2021).
- [48] A. Arrott and J.E. Noakes, *Phys. Rev. Lett.* **19**, 786 (1967).
- [49] W. F. Brown, *Phys. Rev.* **58**, 736 (1940).
- [50] W. F. Brown, *Micromagnetics*, 1st ed., J. Wiley, New York (1963).
- [51] R. F. L. Evans, U. Atxitia, and R. W. Chantrell, *Phys. Rev. B* **91**, 144425 (2005).
- [52] B. J. Hattink, M. García del Muro, Z. Konstantinović, X. Batlle, and A. Labarta, *Phys. Rev. B* **73**, 045418 (2006).
- [53] N. Kalanda, S. Demyanov, M. Krupa, and S. M. Konoplyuk, *Phys. Status Solidi B* **259**, 2200021 (2022).
- [54] J.-F. Wang, Z. Li, X.-J. Xu, Z.-B. Gu, G.-L. Yuan, and S.-T. Zhang, *J. Am. Ceram. Soc.* **97**, 1137 (2014).

Synthesis and structural Characterization of Cu Substituted SrCoO_{3-δ} Perovskite Oxides

Lynda Djoudi^{1,*}, Belkis Bourmal² and Mahmoud Omari¹

¹Laboratory of Molecular Chemistry and Environment, University Mohamed Khider of Biskra, 07000 - Algeria

² Department of Science Material, chemistry, Faculty of Exact and Natural Sciences, University Mohamed Khider of Biskra, 07000 – Algeria

* Corresponding author, e-mail address: lynda.djoudi@univ-biskra.dz

Received 26 July 2022; accepted 16 November 2022; published online 20 December 2022

ABSTRACT

In this work, SrCo_{1-x}Cu_xO_{3-δ} perovskite-type metal oxides (x = 0.00, 0.1, 0.2, 0.3) were prepared by sol-gel method using citric acid as chelating agent. We have focused on examining the effect of partial substitution of cobalt by copper on the phase purity and crystallinity of the end products. The samples obtained after calcination at 900°C for 6h were characterized by X-ray diffraction (XRD), Fourier transform infrared spectroscopy (IRTF) and powder size distribution (PSD).

XRD patterns indicate that a perovskite structure with rhombohedral system has been obtained for all the compositions with no detectable secondary phase where the crystallite size ranges from 48.74 to 53.49 nm. The crystallite size decreases with increasing the copper amount. The grain size of oxides as determined from laser diffraction ranges from 0.213 to 0.307 micron, this result reveals that agglomerates are present in the suspension. Infrared spectroscopy shows a broad characteristic band of absorption observed around 581 cm⁻¹ was attributed to the BO (Co-O, Cu-O) stretching vibration. This band is characteristic of the perovskite structure ABO₃.

1. INTRODUCTION

Perovskite oxides, with a general formula of ABO₃, have been a research hot spot due to their considerable reserves of raw metals and flexible adjustability [1-3]. It is an effective strategy to adjust the physicochemical properties of the perovskite by partial substitution of the A-site or B-site metals [4-7]. Depend on this compositional diversity and adjustable properties, perovskite oxides have been tried to be applied in a great many of fields, including solid oxide fuel cells, metal-air batteries, and oxygen permeation membranes [8-10].

Perovskite-type mixed ionic and electronic conducting (MIEC) materials have high flexibility to tune their physical properties such as oxygen vacancies, structural symmetry, lattice free volumes and metal-oxygen bonding energies.

These properties are strongly dependent on crystal structure and significantly affect electrochemical kinetic properties and stability of the materials [11, 12].

Strontium cobaltite (SrCoO_{3-δ}) is a typical perovskite MIEC showing high electrical conductivity and electrocatalytic property as a cathode material for solid oxide fuel cell (SOFC) and has been widely used as a parent compound to derive other high performance MIEC cathodes [13]. Depending on annealing temperature and oxygen partial pressure during synthesis/fabrication process, SrCoO_{3-δ} may adopt a variety of crystal structures, e.g., orthorhombic, tetragonal and cubic. For example, SrCoO_{3-δ} forms an oxygen vacancy-ordered orthorhombic brownmillerite phase below 653 °C and will transfer to a 2-H type hexagonal phase between 653 and 920°C, eventually changes to a cubic or tetragonal

perovskite phase above 920 °C. However, the high temperature phase will transit reversibly to a hexagonal phase as temperature drops from a high (> 920°C) to intermediate temperature range [14].

In this work, SrCo_{1-x}Cu_xO_{3-δ} perovskite-type metal oxides (x = 0.00, 0.1, 0.2, 0.3) were prepared by citrate sol-gel method. We have focused on examining the influence of copper concentration on the phase purity and crystallinity of the end products.

2. EXPERIMENTAL PROCEDURE

2.1. Powder Synthesis

All the solvents and chemicals were of analytical grade and used without any further purification. A sol-gel route with citric acid was adopted to synthesize SrCo_{1-x}Cu_xO_{3-δ} nanoparticles with x = 0.00, 0.1, 0.2, and 0.3. An estimated quantity of Sr(NO₃)₂, Co(NO₃)₂·6H₂O and C₆H₈O₇, H₂O were dissolved separately in distilled water with magnetic stirring for 15 min. Afterward, the mixture was vigorously stirred on a hot plate at 80 C° for 4 h. The viscous gel was further dried for 12 h at 110 C° in an oven and ground into powder. Subsequently the powder was calcined for 6 h in air at 900 C°. In a similar process, the SrCo_{1-x}Cu_xO_{3-δ} nanoparticles were synthesized by following the above defined steps of sol-gel

method. The estimated amount of dopant copper nitrate was added in the precursor solution and other conditions of synthesis were kept unchanged.

2.2. Characterization

The eventual presence of organic material after calcination was determined by infrared spectroscopy within the interval from 4000 to 400 cm⁻¹ using FT-IR SHIMADZU 8400S spectrometer. The sample was mixed with dry KBr to form a pellet for the measurement. X-ray diffraction (XRD) patterns were carried out with a D8 ADVANCE-BRUCKER using a Cu Kα radiation (λ_{Kα} = 1.54056 Å) and a Ni filter. The powder samples were mounted on a flat XRD plate and scanned at room temperature in the range 10°- 90° to identify the crystalline phases present in the calcined powders by comparison with Joint Committee on Powder Diffraction Standards (JCPDS) files. The crystallite size (D) was evaluated from the broadening of the X-ray diffraction peaks using Scherrer's formula. The average particle size distribution was determined using the laser diffraction method fitted with a wet sampling system (Malvern, Mastersizer 2000).

3. RESULTS AND DISCUSSION

3.1. Infrared Spectra

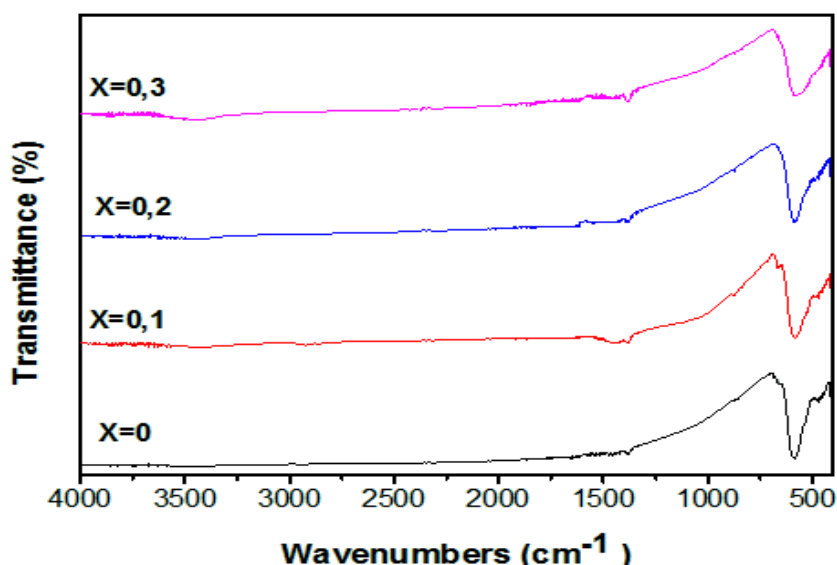


Figure 1. FT- IR absorption spectra of SrCo_{1-x}Cu_xO_{3-δ} (x = 0.0-0.3).

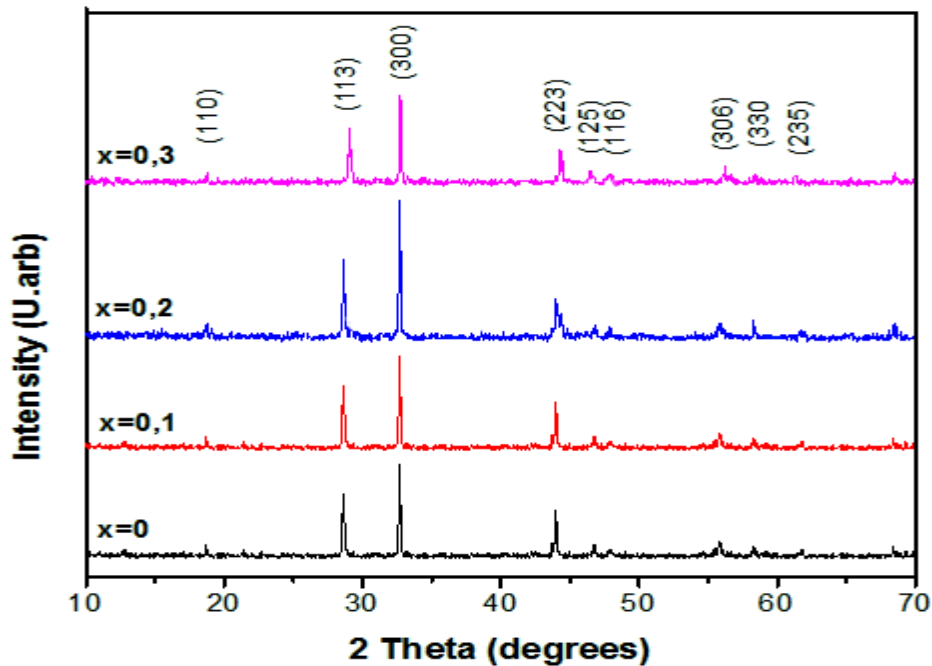


Figure 2. X-ray diffraction patterns of perovskite samples $\text{SrCo}_{1-x}\text{Cu}_x\text{O}_{3-\delta}$ ($x = 0.0-0.3$).

IR analysis of synthesized samples is important both for the control of the reaction process and the properties of materials obtained. The infrared spectra of the $\text{SrCo}_{1-x}\text{Cu}_x\text{O}_{3-\delta}$ samples (Figure 1) are presented in the $400-4000\text{ cm}^{-1}$ region of the IR spectrum. The higher frequency band around 581 cm^{-1} was assigned to the B–O stretching vibration mode (possible Co–O or Cu–O stretching

frequencies vibrations). This band is characteristic of the perovskite structure ABO_3 [15]. No specific peaks of inorganic residues were observed suggesting the high purity of the resulting powders. These results are in accordance with the XRD analysis (Figure 2) which confirmed the formation of only crystalline phase in $\text{SrCo}_{1-x}\text{Cu}_x\text{O}_{3-\delta}$ nanopowders.

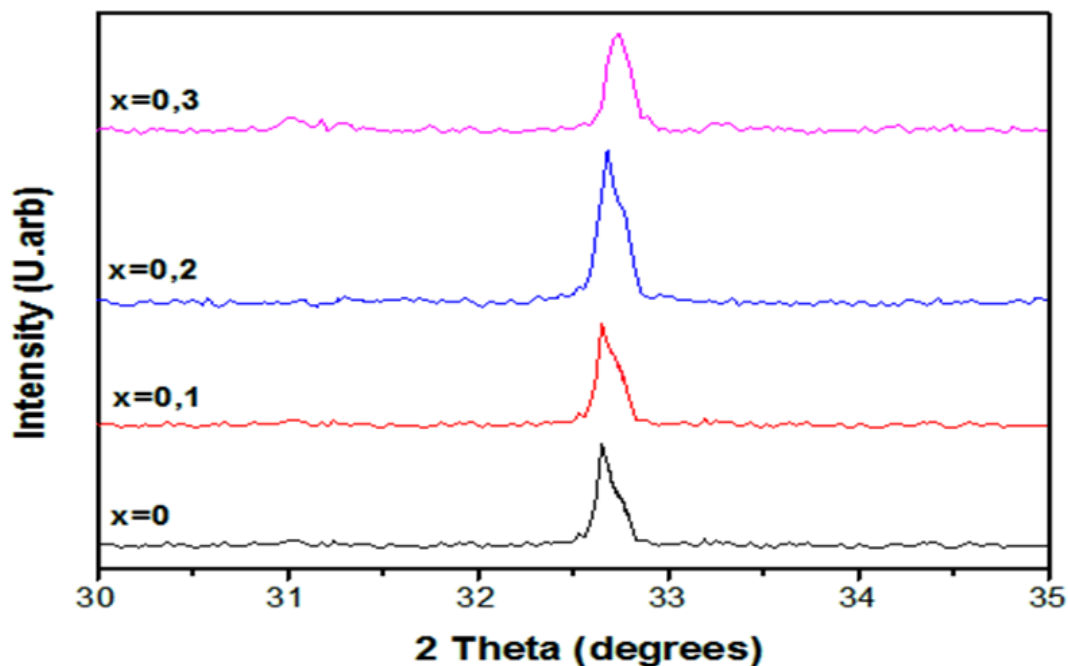


Figure 3. XRD patterns of $\text{SrCo}_{1-x}\text{Cu}_x\text{O}_{3-\delta}$ with enlarged view around (300).

Table 1. Lattice parameters for $\text{SrCo}_{1-x}\text{Cu}_x\text{O}_{3-\delta}$.

Cu content x	a=b (Å)	c(Å)	V(Å ³)
x=0	9.4890	12.3650	964.2
x=0.1	9.4845	12.3637	963.435
x=0.2	9.4797	12.3493	962.656
x=0.3	9.4788	12.3456	961.117

3.2. Structural characterization

The XRD patterns of the catalysts powders $\text{SrCo}_{1-x}\text{Cu}_x\text{O}_{3-\delta}$ ($x=0, 0.1, 0.2, 0.3$) obtained by citrate sol-gel method after calcinations at 900 °C for 6 h summarized in Figure 2, were compared to the relevant data in the Data Bank available in the diffractometer. We observed that all the diffraction peaks matched well with the rhombohedral structure of pure $\text{SrCoO}_{3-\delta}$. They are in excellent accord with JCPDS card 00-049-0692. The pattern clearly indicates the absence of any kind of impurity phases. This shows the proper incorporation and dispersion of Cu^{2+} ions into the $\text{SrCoO}_{3-\delta}$ matrix.

The magnified view around 2θ 30 and 35 was shown in Figure 3. With increase Cu concentration, XRD peak shifted slightly toward a higher 2θ angles (right shift), which demonstrated that the

Cu^{2+} ion was successfully incorporated into the lattice of perovskite structure.

The lattice parameters of the perovskites $\text{SrCo}_{1-x}\text{Cu}_x\text{O}_{3-\delta}$ were calculated for each x value from the XRD patterns using Celref programme. The values of a and c cell parameters (Å) versus the degree of substitution x are given in Table 1.

The values of the lattice parameters decrease with the increasing copper content in the samples from 0 to 0.3 (Table 1 and Figure 4). Such a decrease is also a confirmation for the Cu (II) substitution to Co (II) in the $\text{SrCoO}_{3-\delta}$ crystal lattice. The substitution of Co^{2+} ions ($r_{\text{Co}^{2+}} = 0.745$ Å) by smaller Cu^{2+} ions ($r_{\text{Cu}^{2+}} = 0.73$ Å) [16] led to the reduction of the unit cell parameters. A similar observation was found in $\text{SrCo}_{1-x}\text{Ni}_x\text{O}_{3-\delta}$ systems [17].

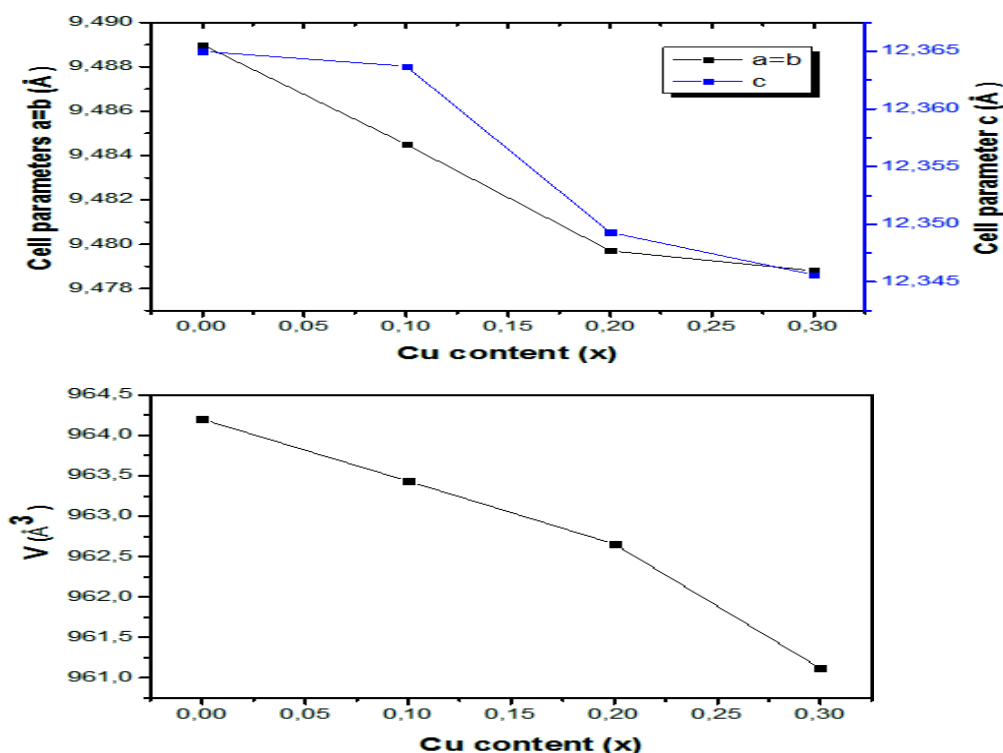


Figure 4. Evolution of lattice and volume parameters a function of copper content.

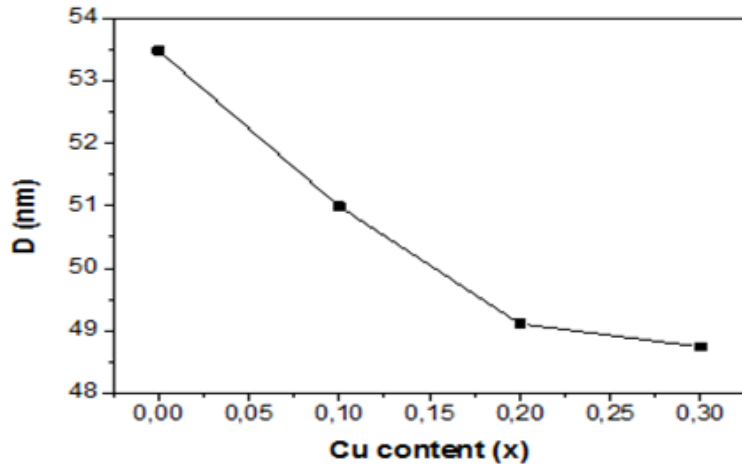


Figure 5. Crystallite size of SrCo_{1-x}Cu_xO_{3-δ} powders (x = 0.0-0.3).

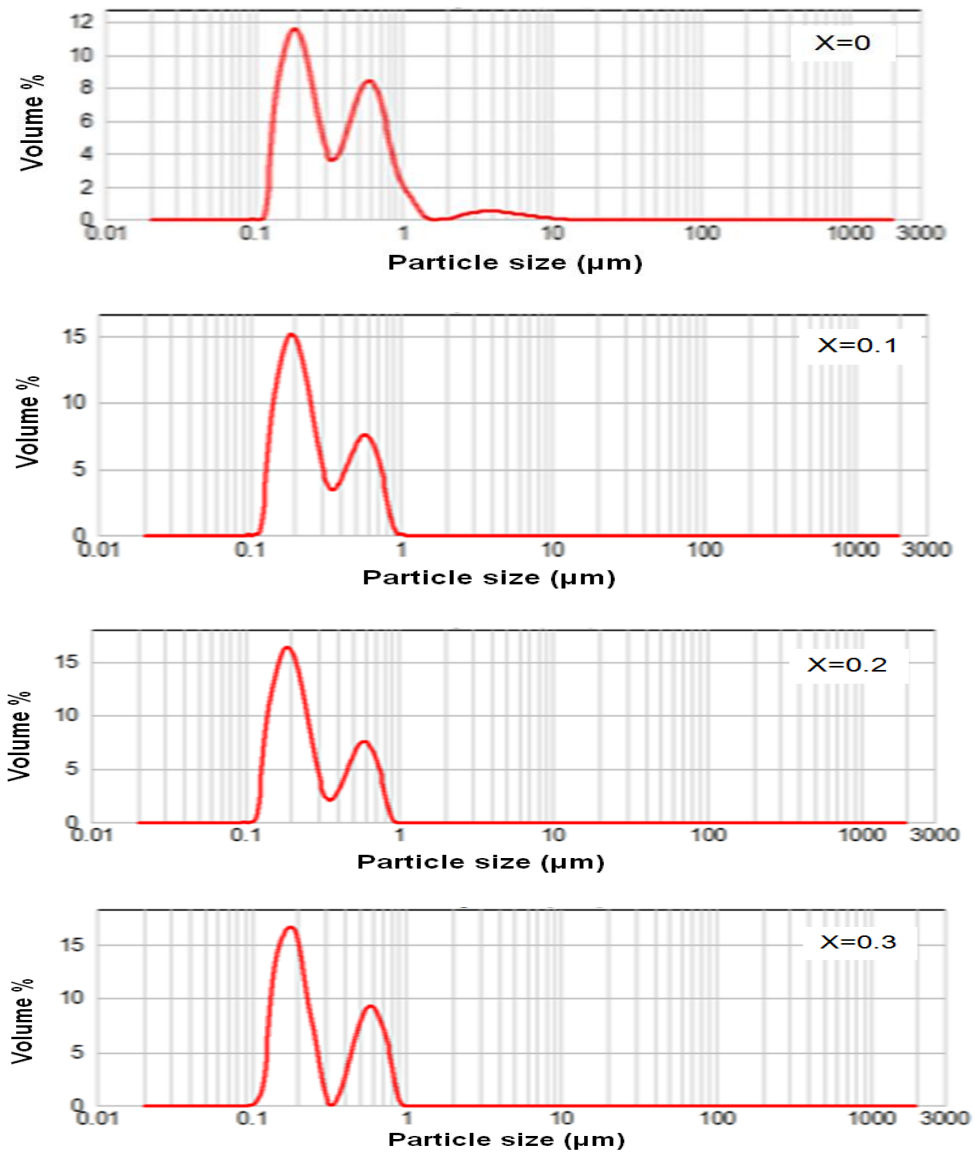


Figure 6. Particle size distribution of samples SrCo_{1-x}Cu_xO_{3-δ} with x=0, 0.1, 0.2, 0.3.

Consequently, the cell volume gradually when the substitution x increases from 0 to 0.3 (Figure 4) are due to the significant decrease in the parameters a and c .

3.3. Crystallite size and distribution by volume particle size of $\text{SrCo}_{1-x}\text{Cu}_x\text{O}_{3-\delta}$ powder

The average crystallite size (D) was evaluated from the broadening of the XRD line width by applying the Scherer's formula (Figure 5). It is observed that crystallite size decreases with increasing copper content. This is probably due to the incorporation of Cu^{2+} into the $\text{SrCoO}_{3-\delta}$ lattice which leads to the crystallite decrease.

Figure 6 shows that the particle size distribution in volume of $\text{SrCo}_{1-x}\text{Cu}_x\text{O}_{3-\delta}$ samples with $x=0, 0.1, 0.2$ and 0.3 , the average diameters in volume $D_v(0.5) = 0.307; 0.236; 0.225; 0.213 \mu\text{m}$ respectively. This result also indicates that the powders are highly agglomerated. This is could be due to the agglomeration of ultra-fine powders, present in the suspension.

4. CONCLUSIONS

Four powders with nominal composition $\text{SrCo}_{1-x}\text{Cu}_x\text{O}_{3-\delta}$, ($x = 0, 0.1, 0.2, 0.3$) have been synthesized by citrate sol-gel method. XRD patterns indicate that a stable perovskite phase with rhombohedral system has been obtained for all the compositions with no detectable secondary phase as confirmed by XRD and FT-IR. The crystallite size decreases with increasing the copper amount. The grain size of oxides as determined from laser diffraction is between 0.213

and 0.307 micron. This result reveals that agglomerates are present in the suspension.

REFERENCES

- [1] Grimaud, A., et al. *Nature Communications* **4**, 2439-2441(2013).
- [2] Jung J I, Jeong H Y, Kim M G, et al. *Advanced Materials* **27**,266-271(2015).
- [3] Lin Y, Ran R, Chen D, et al. *Journal of Power Sources* **195** , 4700-4703(2010).
- [4] Ludwig J. *Journal of Power Sources* **155**, 23-32 (2006).
- [5] Du Z, Yang, Peng, Wang, Long, et al. *Journal of Power Sources* **265** , 91- 96 (2014).
- [6] Shimizu, Y. Matsuda, H. Miura, N. Yamazoe. *Chem. Lett.* **21**, 1033–1036 (1992).
- [7] Duan, Y. Sun, S. Xi, S. Ren, X. Zhou, Y. Zhang, G. Yang, H. Du, Y. Xu, Z. *J. Chem. Mater.* **29**, 10534–10541(2017).
- [8] S.P. Jiang. *Journal of Materials Science* **43** (21), 6799–6833 (2008).
- [9] Xin S, Dong D, Parkinson G, et al. *Journal of Membrane Science* **454** ,444-450 (2014).
- [10] Shao Z.P., Haile S.M. *Nature* **431**, 170–173 (2004).
- [11] J. Richter, P. Holtappels, T. Graule, T. Nakamura and L. J. Gauckler. *Monatshefte für Chemie-Chemical Monthly.* **140**, 985-999 (2009).
- [12] A. F. Sammells, R. L. Cook, J. H. White, J. J. Osborne and R. C. MacDuff, *Solid State Ionics* **52**, 111-123 (1992).
- [13] D. Chen, C. Chen, Z. Zhang, Z. M. Baiyee, F. Ciucci and Z. Shao, *ACS Appl.Mater.Interfaces* **7**, 8562-8571 (2015).
- [14] C. De la Calle, A. Agüero, J. Alonso and M. Fernández-Díaz, *Solid State Sci.* **10**, 1924-1935 (2008).
- [15] Hongtao Cui, Marcos Zayat, David Levy. *Journal of Non-Crystalline Solids* **352**, 3035–3040 (2006).
- [16] R.D. Shannon. Revised effective ionic radii and systematic studies of interatomic distances in halides and chalcogenides, *Acta Cryst.* **A32** 751-767(1976).
- [17] Makhloufi S. and Omari M. *J. Inorg. Organomet. Polym.* **26**, 32, (2016).

Conductivity and transmittance enhancement of PEDOT:PSS thin films by graphene addition

Felipe Teixeira Mabilia*, Shu Hui Wang

University of São Paulo, Polytechnic School, Department of Metallurgical and Materials Engineering, Av. Professor Mello Moraes, 2463, CEP: 05508-030, São Paulo/SP, Brazil

**Corresponding author, e-mail address: felipe.mabilia@usp.br*

Received 17 June 2022; accepted 16 November 2022; published online 20 December 2022

ABSTRACT

Compared to conventional inorganic semiconductors, organic semiconductors present several advantages, such as cost-effectiveness, mechanical toughness, synthesis versatility and simple production set-ups, among others. In this work, we have prepared conductive solid films based on multilayer graphene (mG) and poly(3,4-ethylenedioxythiophene):polystyrenesulfonate (PEDOT:PSS) from liquid dispersions. mG-10.6 wt% dispersion in isopropanol was prepared in two steps. In the first step, graphite was submitted to liquid phase exfoliation in N-methyl-pyrrolidone (NMP) (5.3 wt% of mG), then, in the following step, NMP was removed by precipitation and mG redispersed, using polyethyleneimine and acetic acid-1M in isopropanol, respectively. The nanocomposite films were prepared from dispersions of mG and PEDOT:PSS, by spin-coating, to reach pre-established solid concentrations of 10.2 wt% and 49.9 wt% of mG. The optical and electrical properties of the thin films were characterized using UV-Visible Spectroscopy and an adapted four-probe resistance measurement, while Raman Spectroscopy, Scanning Electron Microscopy (SEM), and Atomic Force Microscopy (AFM) were applied to analyze their morphological features. The thin films showed high transmittances, even multilayer, upholding more than 85% for three-layer films, similar to that found in the single-layer ones. The sheet resistances of the films were detected in the range of a few hundreds of Ω/\square . Both transmittance and sheet resistance of the films were improved when compared to those found in pristine mG and pristine PEDOT:PSS, which is due to higher charge mobility in the nanocomposite. Raman Spectroscopy showed the formation of the composite by π - π interaction and the conformational change in the polymer chains was confirmed by peak shift. SEM analysis showed that the films are largely homogeneous, and mG is uniformly dispersed, nevertheless the mG platelets appear to be standing up from the film (AFM). The phase image (AFM) allows the differentiation between rigid and soft regions, i.e., mG/PEDOT and PSS, respectively. Semiconductive nanocomposites having high load of mG were successfully prepared, and their resulting electrical and optical properties make them suitable to be used, e.g., as transparent electrodes, in the fabrication of displays, lighting devices and photovoltaic materials or as multipurpose conductive inks.

1. INTRODUCTION

Conductive transparent electrodes (TCEs) have high electrical conductivity, low sheet resistance and transparency to visible light [1,2], essential characteristics for organic solar cells (OPVs), displays, organic light-emitting diodes (OLEDs), liquid crystal displays, touch displays, lasers [3] and electrochromic devices [4], among other applications. The most common material used in the production of TCEs is indium tin oxide (ITO),

however alternative materials have been investigated to replace ITO due to the high cost and scarcity of indium. Additionally, ITO thin films are fragile, making them difficult to be used in the manufacture of flexible devices, do not adhere well to polymeric materials, require high temperatures and high vacuum for their manufacture, and have low chemical resistance to acidic and alkaline environments [1-8].

Metallic nanowires, carbon nanotubes, graphene and conductive polymers have been

suggested as possible replacements for ITO [1-7]. Poly(3,4-ethylenedioxythiophene):poly(styrene-sulfonate) (PEDOT:PSS) is a polymer blend commercially available as aqueous dispersion which is solution processable and forms a highly flexible, light-transparent, thermally stable film, commonly used as a transparent hole transport layer in OLEDs and OPVs [2,4]. However, PEDOT:PSS thin films require improvements in conductivity to be viable in certain applications as TCE [7]. Due to its low cost and easiness to form thin films with excellent properties, there is a great academic and technological interest in increasing its conductivity. Modifications were carried out, such as the addition of organic solvents to the dispersion before the deposition of the films [4,7,9,10], treatments of formed films [1,3,5,7] with solvents or acids or even incorporation of conductive nanoparticles, forming nanocomposites, among which composites with graphene [11], graphene oxide [12], graphene quantum dots [13], and carbon nanotubes [2] stand out.

Graphene is a material composed of carbon atoms arranged in a two-dimensional structure in a honeycomb lattice [14-16]. The conjugation of π bonds results in excellent electrical properties, making graphene an interesting option for the production of electronic devices, even as an additive in composites [14]. In addition, graphene presents high electronic mobility, high transparency, flexibility and stability, qualifying it for electronic applications [17]. On the other hand, the difficulty of producing quality graphene on a large scale is a disadvantage for the use of this material. Mechanical exfoliation of graphite produces the best samples, but it is not easily scalable. Liquid-phase exfoliation of graphite is an inexpensive and scalable production method of graphene, which

consists of adding graphite to solvents such as N-methylpyrrolidone (NMP), isopropyl alcohol (IPA) or dimethylformamide (DMF) and dispersing the graphene sheets with the aid of sonication [18,19].

Exfoliated graphenes in composites with PEDOT:PSS [11] increased the conductivity from 0.16 S/cm to 60 S/cm for 0.47% by weight of graphene, with transmittances above 90% [11]. Hong et al. [20] produced PEDOT:PSS/graphene composites from an aqueous dispersion of graphene and used the resulting composite films as counter electrodes for dye-sensitized solar cells. The transmittance was over 80% and the energy conversion efficiency was 4.5% under white light at 100 mW AM 1.5 [20]. Hilal and Han [21] obtained graphene dispersed in NMP after a series of steps and produced composite films of PEDOT:PSS/graphene with different concentrations of the nanomaterial, obtaining sheet resistances lower than $10 \Omega/\square$ and transmittances above 70% when deposited on ITO/glass [21]. Park et al. [22] produced hybrid PEDOT:PSS/graphene films by depositing PEDOT:PSS films on graphene films, obtaining sheet resistances of about $100 \Omega/\square$ and transmittances above 80% [22].

In this work multilayer graphene produced by exfoliation in NMP (mG_NMP) was used to prepare PEDOT:PSS/mG composite films, which were characterized by Raman Spectroscopy, UV-Visible Spectroscopy, Scanning Electron Microscopy (SEM), Atomic Force Microscopy (AFM) and electrical conductivity measurements. The results have shown their potential application as TCEs and conductive inks.

2. MATERIALS AND METHODS

2.1. Powder Synthesis

Table 1. Compositions of the mG and PEDOT:PSS/mG dispersions.

Dispersion	mG_NMP mL	PEI mL	HAc_IPA 1 M mL	D2 μ L	PEDOT/PSS μ L	DMSO μ L	Solids mg/mL	PEI wt%	mG wt%	PEDOT/PSS wt%
D1	10	1.1	5	-	-	-	10.7	2.1	97.9	-
D2	10	0.42	5	-	-	-	10.6	0.8	99.2	-
D3	-	-	-	420	400	100	9.6	0.4	49.9	49.3
D4	-	-	-	95	800	200	9.0	0.08	10.2	89.7
DP	-	-	-	-	1600	400	8.8	-	-	100
DP*	-	-	0.16	-	1600	400	8.8	-	-	100

Table 2. Film deposition parameters.

Film	Dispersion	Speed	Time (s)	Layers
1	D1	200	20-60	1
2	D2	500	20-50	1;3
3	D3	500	30	1
4	D3	1000	30	1
5	D4	1000	30	1;3
6	D4	500	30	2
7	DP	500-1000	20-30	1
8	DP*	500-1000	20-60	1

The initial graphene dispersion (mG_NMP) was prepared from the heat treatment of graphite (Nacional de Grafite), followed by exfoliation in NMP aided by an ultrasonic bath [23]. After 220 hours in the ultrasonic bath (Quimis, model Q335D), the dispersion was centrifuged and filtered to separate the undispersed fraction. The concentration of graphene present in the dispersion determined by gravimetry was 5.25 ± 0.35 mg/mL.

Two dispersions of graphene (D1 and D2) in isopropanol (IPA) (Table 1) and two dispersions of PEDOT:PSS/mG (D3 and D4) in IPA (Table 1) were prepared.

Graphene dispersions in IPA were prepared from mG_NMP using a solution of polyethyleneimine in IPA (PEI, 1 mg/ml). D1 was prepared by adding 1.1 mL of PEI in IPA (1 mg/mL) to 10 mL of mG_NMP, followed by centrifugation, washing the precipitate with distilled water, and centrifugation again, the process was repeated three times. The precipitate was redispersed in 5 mL of HAc in IPA (1 M) and portions of 10 μ L of HAc were added until mG is completely dispersed. The D2 dispersion was prepared using a similar procedure, but the quantities of the components were changed, as shown in Table 1.

D3 and D4 were prepared from D2 and PEDOT:PSS (Sigma Aldrich, code 483095). For D3, 0.4 mL of PEDOT:PSS was added to 0.42 mL of D2, followed by 0.1 mL of DMSO. D5 followed the same procedure, changing the volumes to 0.095 mL of D2, 0.8 mL of PEDOT:PSS and 0.2 mL of DMSO (Table 1). DP is a graphene-free PEDOT:PSS dispersion prepared by mixing 1.6 mL of PEDOT:PSS with 0.4 mL of DMSO in an

ultrasound bath. DP* is analogous to DP, but has received HAc in IPA to aid surface wetting.

All dispersions were kept for one hour in the ultrasonic bath before film deposition to avoid the presence of possible aggregates. The dispersions were deposited on glass substrates previously cleaned with a glass cleaner (Aquabrilho®, Adespec, Brazil). This procedure aimed to increase the adhesion of the films to the substrate without the need to go through all the steps using detergent, acetone and IPA, usual in traditional glass cleaning. The depositions were carried out in a spin coater (Swin 4", model EC4 SYN 3S102-0902). The dispersion volume used was 70 μ L, except for DP and DP* dispersions, for which the volume varied between 70 μ L and 160 μ L. Annealing was performed on a heating plate (Yotec, model YS-200S) at 120 °C during 20 minutes. The parameters used in the deposition are summarized in Table 2.

A dried thin film deposited on a glass slide was used for the characterization of mG_NMP by Raman spectroscopy, according to a previous work [24]. To evaluate the graphene after redispersion in IPA with the addition of PEI and HAc, as well as the composites and the interaction between graphene and PEDOT:PSS, Raman spectroscopy was performed using the WITec Confocal Raman Microscope (Alpha 300R model) with 532 nm (green) laser and maximum power of 45 mW. Due to the nature of the samples, it was chosen to use a lower power, of only 8 mW, to avoid any alteration in the analyzed materials.

The electrical resistance of the films was measured using a method similar to the four-probe method, but with a device with flat contacts to avoid damaging the films. A Keithley 2400 multimeter

was used to measure electrical resistance, which was used to calculate the sheet resistance of the films. The reported values refer to the average of 9 measurements.

A scanning electron microscope (FEI, Inspect F50) was used to analyze the solid films of D2 on a glass substrate and D4 on silicon (0.1 mL, 500 rpm) and mica. A thin layer of gold was deposited on the samples with glass and mica substrate before analysis.

Transmittance was measured using a UV-Vis Spectrophotometer (Cary 50 Conc). Part of the film was removed from the sample and the region was used as reference (blank). The wavelength range

was from 300 nm to 800 nm. Transmittance values refer to measurements collected at 550 nm.

Atomic force microscopy (Multimode 8, Bruker) was performed in tapping mode. Films from D2 (AFM1), D3 (AFM3) and D4 (AFM2 and AFM4) were analyzed. Samples AFM1 and AFM4 are 3-layer film, while AFM2 is monolayer and sample AFM3, 2-layer. To measure the thickness of the samples, a small portion of the films was removed to create a step with the aid of a wooden toothpick.

3. RESULTS AND DISCUSSION

3.1. Raman Spectroscopy

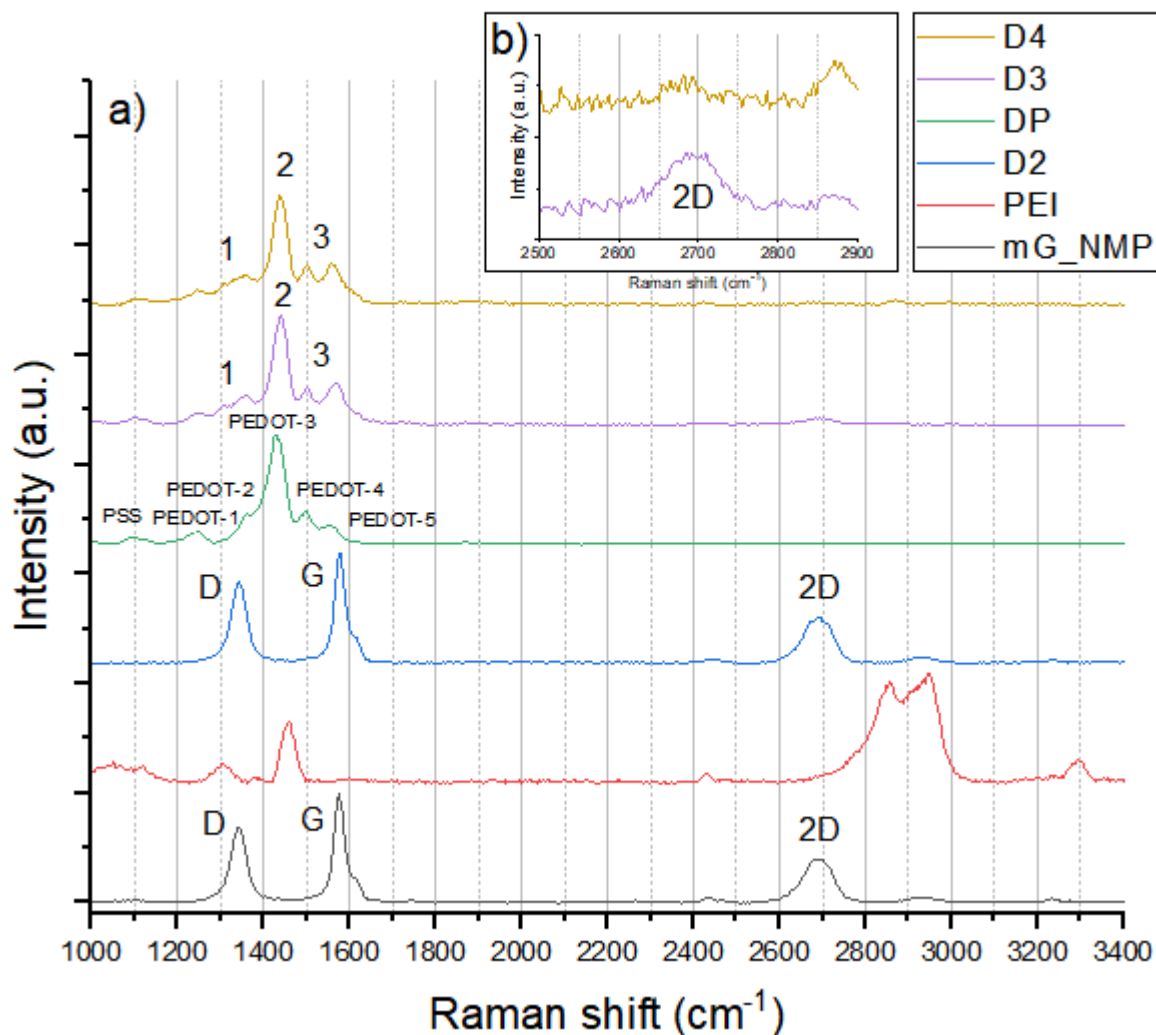


Figure 1. Raman spectra of a) mG, DP, PEI, D2, D3 and D4 and b) D3 and D4 in the 2D region (2500 cm^{-1} - 2900 cm^{-1}) magnified $\sim 13\times$.

Films containing mG were characterized by Raman spectroscopy according to a previous work [24], and the position of the peaks, the ratios between the intensities of the D and G peaks (I_D/I_G) and 2D and G (I_{2D}/I_G) were determined and analyzed. The results allowed us to conclude that the graphenes present in the original mG_NMP dispersion have two to five layers. The D peak is present due to sp^2 -carbon atoms at the edge of the graphene sheets, in arm-chair configuration [25], which is activated by the presence of defects [26]. The G peak results from the stretching of C-C bonds in the hexagonal basal plane. The 2D band comes from the second order vibration of D phonons [27].

Note that the mG_NMP and D2 spectra are practically identical, despite the small peak shifts, indicating that the redispersion in IPA with the aid of PEI and HAc allowed increasing the graphene concentration without significantly altering its characteristics. The ratios (I_D/I_G) and (I_{2D}/I_G) are equal to 0.74 and 0.44, respectively, for D2, while for mG the values were 0.69 and 0.41 [24], reinforcing that the material did not suffer major changes after redispersion. For mG and D2, the D peak is at 1346 cm^{-1} . The G peak, on the other hand, presents a displacement of 4 cm^{-1} from mG_NMP to D2, from 1579 cm^{-1} to 1583 cm^{-1} . Finally, the 2D band shifts from 2686 cm^{-1} to 2700 cm^{-1} from mG to D2. It is important to note that here the 2D is a broad band and the mentioned value corresponds to its peak. The spectrum of mG_NMP can be seen in Figure 1, allowing comparison with the spectrum of graphene redispersed in D2.

The DP spectrum (Figure 1) is typical of this material [28] and, as it represents $\leq 2.1\text{ wt}\%$ in the films (Table 1), it has little or no influence on the spectra of D2, D3 and D4.

The DP spectrum (Figure 1) has an usual appearance for the PEDOT:PSS blend, according to the literature [7,29-31]. The only PSS visible band is located at $1070\text{-}1170\text{ cm}^{-1}$ and is due to the presence of sulfonic acid and sulfonate groups [29,32], and caused by a complex deformation mode, with the distribution of potential energy associated with the stretching of the C-S+C-C+SO₃ bond that presents increased downshift as the ionization degree rises [33]. The absorption bands of PEDOT are intense and here they are labeled as PEDOT-1 to PEDOT-5 to facilitate their identification. The PEDOT-1 peak (1246 cm^{-1}) is

caused by the inter-ring stretching of C α -C α' ; PEDOT-2 (1367 cm^{-1}), to the stretching of the C β -C β bond; PEDOT-3 (1429 cm^{-1}), to the vibration of C α =C β symmetrical, while C α =C β asymmetrical is responsible for PEDOT-4 (1502 cm^{-1}) [31]; finally, PEDOT-5 (1555 cm^{-1}), originates from the antisymmetric stretching of C=C [32,34] on the thiophene rings at the end and in the middle of the PEDOT chains [35]. It is noteworthy that the addition of DMSO to PEDOT:PSS causes changes in the spectrum in relation to pristine PEDOT:PSS, such as a decrease in the intensity of the PEDOT bands [31] and displacement and narrowing of the most intense peak [7], suggesting a change in the conformation of the chains that leads to better conductivity.

When comparing the DP spectrum with the D3 and D4 spectra (Figure 1), which received the addition of mG, the difference is visible. In region 1 (1200 cm^{-1} to 1400 cm^{-1}) of both spectra, it is noticed that the PEDOT-1 and PEDOT-2 peaks are closer and that the PEDOT-2 peak is more separated from PEDOT-3, due to the contribution of the D peak from D2. Furthermore, the most intense PEDOT-3 peak (region 2, 1400 cm^{-1} to 1500 cm^{-1}) is upshifted (1441 cm^{-1} for D3 and 1437 cm^{-1} for D4) and with a lower intensity. Finally, in region 3 (1500 cm^{-1} to 1600 cm^{-1}), PEDOT-5 became more intense than PEDOT-4, due to the G peak from D2. In the D3 spectrum, at 2700 cm^{-1} , it is possible to see a small bump, due to the 2D peak from D2. It is important to remember that D3 has almost 5 times more graphene than D4. The intensity of the 2D peak in D3 surpasses by far that in D4 (Figure 1b).

The changes in the D3 and D4 spectra compared to the DP spectrum point to the formation of the composite between graphene and PEDOT:PSS, helped by π - π interactions between the aromatic structures of these materials [36,37], as well as possible changes in the PEDOT:PSS chain conformation, promoting more intermolecular π - π interaction that changes the electrical properties of the films [37].

3.2. Sheet Resistance and transmittance

The dispersions containing only mG form films that present emptiness among the particles, so, although graphene has high electrical conductivity,

Table 3. Physical characteristics of the films.

Film type ID	Dispersion	Number of layers	Appearance	%T ^a	SR ^b (kΩ/□)	σ ^c (S/m)
1	D1	1	Non-uniform	77.67 ±0.08	15290 ± 20860	2.18
2.1	D2	1	Relatively uniform	85.52 ±1.32	188260 ± 162840	6.42
2.2	D2	3	uniform	67.51 ±0.48	177880 ± 48840	0.19
3	D3	1	Non-uniform	81.43 ±0.03	2.34 ± 2.70	14245.01
4	D3	1	uniform	87.20 ±2.26	1.46 ± 0.37	22831.05
5.1	D4	1	uniform	93.47 ±0.01	1.07 ± 0.08	31152.65
5.2	D4	3	Non-uniform	88.71 ±1.93	0.41 ± 0.10	20325.20
6	D4	2	Non-uniform	64.60 ±3.55	0.25 ± 0.27	47058.82
7	DP	1	Non-uniform	53.73 ±0.20	1.30 ± 0.41	7692.31
8	DP*	1	Non-uniform	73.20 ±0.04	0.90 ± 0.21	11111.11

^a refers to the film transmittance at 550 nm; ^b the sheet resistance; and ^c the mean conductivity.

the charge flow suffers discontinuity in these void regions, thus higher local voltage might be required to enable charges' jumping to neighboring particles. In composites, PEDOT/PSS works as a semiconductor matrix, facilitating charge transport. Increasing the number of layers also favors the particle packing, assists the lateral π-π interactions and the charges' hopping between the stacked layers.

Sheet resistance and transmittance results are summarized in Table 3. DP-derived films show sheet resistance values in the range of 900 Ω/□ – 1.3 kΩ/□. The D1 film has a high value of sheet resistance, which is explained by the larger amount of insulating PEI. For D2 (films 3.1 and 3.2), the decreased amount of PEI may cause poorer dispersion, generating agglomerates that act as charge traps, thus resulting in higher sheet

resistance compared to D1 (sample 1). The films from D1 and D2 resulted in quite high sheet resistances, explained by the emptiness surrounding the particles, which compromises the charge flow.

The PEDOT:PSS/mG composite films 3 - 6 showed a decrease of up to 6 orders of magnitude compared to films 1 – 2 that contain only mG, from ~188 MΩ/□ to ~250Ω/□. Films 5.1, 5.2 and 6, from D4, also show the influence of the number of layers on the sheet resistance. In addition, film 7 was also produced under a lower rotation speed that is likely to lead to thicker films. The lowest value achieved for film 6, 250 Ω/□, comes at the cost of lower transmittance, ~60%, indicating incremented thickness. Films 5.1 and 5.2 and film 6 used the same dispersion and showed comparable sheet resistance, associated with much higher

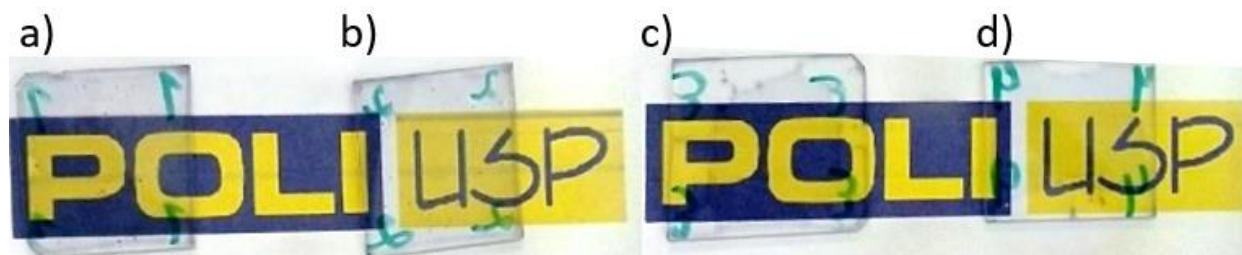


Figure 2. Images of one-layer films prepared by spin-coating, film 4 (a and b) and film 5.1 (c and d).

transmittance values, above 85%, even when more layers were deposited.

Figure 2 shows images of some films 4 and 5.1 that show good reproducibility in the preparation, and exemplify the high transmittance shown in Table 3.

The composite films presented lower resistances compared to those from PEDOT:PSS only, moreover the improvement is still significant, with sheet resistance halving after the addition of mG. Film 7 obtained from DP present several dark spots, discontinuities, and partial coating of the glass. This poor visual uniformity is reinforced by the transmittance results, lower than those found in all other films.

The addition of HAC in IPA to PEDOT:PSS (film 8) slightly improved the uniformity and conductivity of the films, affecting positively its performance. Treatment of PEDOT:PSS films with strong acids is a known technique to improve their conductivity, but it involves washing the films with the acid, not adding them to the dispersion. Liu et al. [4] used acetic acid in isopropanol in mass concentrations between 40% and 100% to treat PEDOT:PSS films, obtaining results of sheet resistance of 0.213 $k\Omega/\square$ for 80% HAC in IPA [4]. Besides, the addition of IPA to PEDOT:PSS promotes wettability and increases the adhesion of the films to the glass, and 50% of IPA reduced the resistivity slightly, according to Borazan et al. [38] this may also explain the higher transmittance of film 8 in relation to films 7 [38].

It is interesting to compare the results of D3 and D4. Although D3 contains almost 5 times more mG than D4, its sheet resistances are higher, possibly due to the presence of mG clusters in D3 films. Films from both dispersions show high transmittances, although minimum dark spots are seen, indicating both mG agglomeration and presence of polymeric gels due to the large sized polymer chains or a non-homogeneous ionization of the PSS [39]. One way to solve this problem is by centrifuging the PEDOT:PSS, prior to deposition, and remove the poor soluble fraction.

The decrease in sheet resistance in composite films can be explained by the presence of conductive graphene in the semiconducting polymer matrix. Yoshida [39] deposited composite films of PEDOT:PSS and conductive silver ink, associating the decrease in the resistivity of the

films with the presence of micrometric silver particles between the polymer chains, aiding the movement of the charge carriers and reducing the energy required for it. It is reasonable to assume that an analogous situation occurs as mG may present segments of dioxythiophene anchored onto its surface, increasing the cohesion of the solid film, provided it is well dispersed. Furthermore, the addition of DMSO alters the conformation of the chains, exposing these dioxythiophene segments by stretching the PEDOT chains, also contributing to the charge mobility [39].

The decrease in the sheet resistance in polymer/graphene composites is attributed to the high conductivity and high electronic mobility of graphene, which acts as a conducting medium for the charges [40-42]. The energy levels' compatibility between PEDOT and graphene contributes to their strong π - π interaction and the electrostatic repulsion between graphene and PSS that supports the formation of homogeneous film [43-46]. According to Kim et al. [45], PEDOT chains are absorbed on the graphene surface, the dioxythiophene groups donate electrons to graphene and increase the concentration of charge carriers, whereas the chains assume a linear or expanded coil conformation. Moreover, due to the intermolecular π - π interactions, the influence of the PEDOT conjugation defects reduces and facilitates charge transfer, decreasing the barrier to their movement. Additionally, the extension of the conjugated π -system increases and the π - π^* band gap narrows, resulting in larger number of charge carriers and higher charge carriers' mobility.

However, increasing the concentration of graphene also represents an increase in the concentration of defects, such as voids in the material, so they will not reflect a continuous increase in conductivity, as such defects are charge traps that will influence the charge concentration and mobility [45]. Therefore, large amount of graphene may also cause aggregation and reduce the conductivity of the films, as in the case of D3.

The conductivities of the films (Table 3) was calculated considering that the thickness of the films are 30 nm for 1 layer, 85 nm for 2 layers and 120 nm for 3 layers for the composites, while 80 nm for 3 layers for mG, and 100 nm for 1 layer of DP

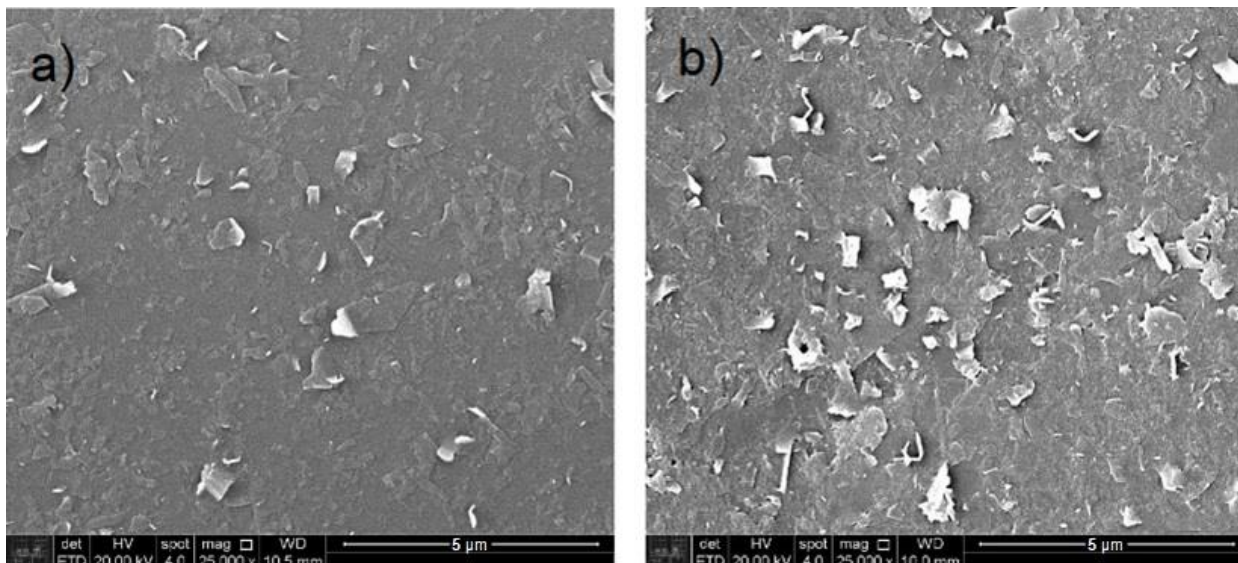


Figure 3. Micrographs with 25000x magnification of the dispersions a) D2 and b) D4.

and DP*. The thicknesses were estimated by AFM, except for DP and DP*, which presented low transmittances. The results indicate that lower values of sheet resistance for thicker films, as expected, is not a rule, in fact, some films present lower conductivity as more layers are deposited, which is exemplified by 2.2 vs. 2.1 or 5.2 vs. 5.1 and 6, demonstrating that for the same composite the inner microstructure (cohesiveness) of the film prevails over the composition regarding the mobility of the charge carriers.

TCEs have several applications, each with its specific requirements. Transmittance values usually vary between 86% and 92% and sheet resistance values can range from 30 Ω/\square to 1500 Ω/\square [47], so the films obtained from D3 and D4 are potential candidates in this kind of application.

The results presented here are comparable to sheet resistance results reported in the literature. Li et al. [48] prepared PEDOT:PSS/graphene composites from an aqueous slurry of graphene and obtained films with transmittances of about 90% and sheet resistances between 1902 Ω/\square and 2980 Ω/\square . Uz et al. [49] manufactured graphene films with a sheet resistance of 200 Ω/\square , suggesting its use in biomedical applications. Fang and his group [50] manufactured PEDOT:PSS/graphene films by spin and blade coating on PET substrates, with the best results being 80.6% transmittance with a sheet resistance of 731 Ω/\square and 85% of transmittance with a sheet resistance of 1783 Ω/\square .

Thus, given their electrical and optical properties, the composites developed in this work can be used as TCEs. Another suggested application for these materials is in conductive trails.

3.3. Scanning electron microscopy

Figure 3 shows two SEM micrographs at 25000x magnification. No significant differences are observed between mG films and mG/ PEDOT:PSS composite films. It is noted in both images, the mG sheets “popping out” of the films, this effect being greater in D4, which seems to present higher roughness. In Figure 3a, it can be seen that mG is extensively well dispersed, but the electrical measurements have shown that there is no effective conductive medium between the sheets, since this sample is from D2, only mG film. Figure 3b shows a D4 composite film, mG dispersed in PEDOT:PSS matrix, in which, apparently, there are conductive paths for the charge carriers (Table 3). The discrete emptiness between the sheets in D2, which is responsible for the low electrical performance, is not observable under SEM. We believe that the composites can be improved by using smaller amounts of mG as additive in order to avoid aggregation that serves as charge traps, a factor that is even more relevant when considering D3, which has 5 times more mG than D4.

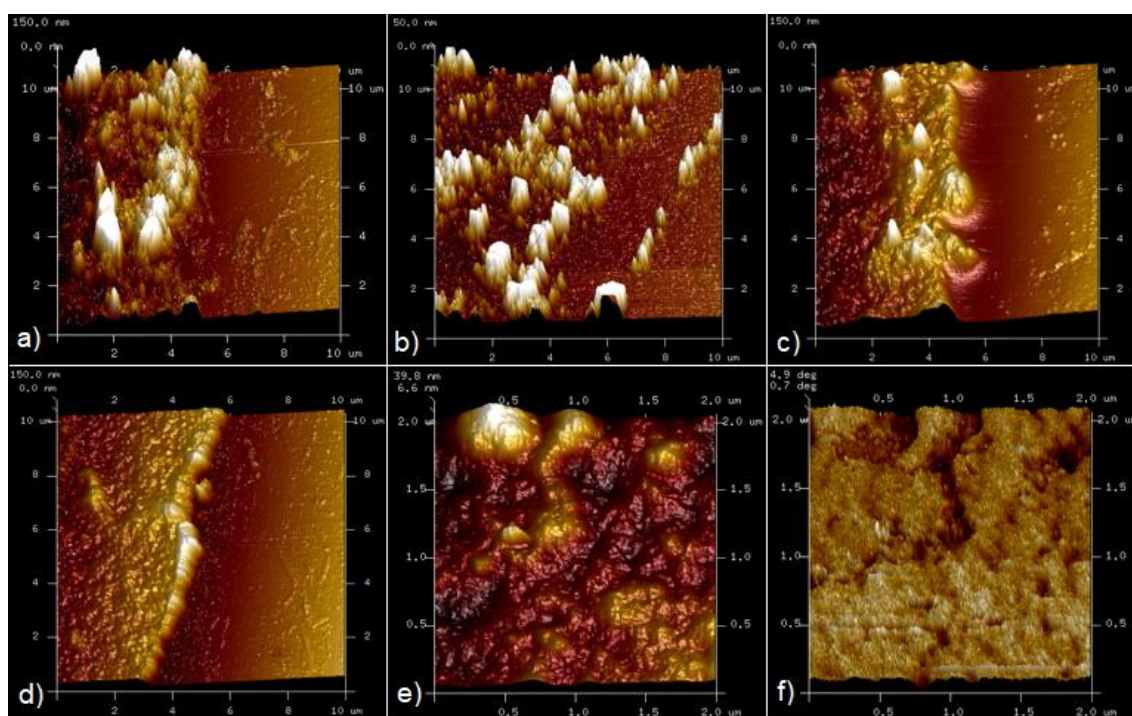


Figure 4. AFM images of films. a) Step region of sample AFM1 (D2, 3-layer, 81 nm); b) Step region of sample AFM2 (D4, 1-layer, 29 nm); c) Step region of sample AFM3 (D3, 2-layer, 85 nm); d) Step region of sample AFM4 (D4, 3-layer, 117 nm); e) Magnification of the surface of sample AFM4; and f) Phase image of sample AFM4.

3.4. Atomic Force Microscopy

Figures 4a - 4d show the step regions in which the film thicknesses were measured. Figure 4a corresponds to the sample AFM1 (D2) with a thickness of 81 nm. Figure 4b corresponds to the AFM2 sample (D4) with a thickness of 29 nm. When comparing this result to the thicknesses values of samples AFM3 (D3) and AFM4 (D4) (Figures 4c and 4d, respectively), we observed that the deposition of a new layer of composite film onto an existing layer, in fact, does not contribute equally to the thickness, reaching 85 nm and 117 nm, respectively. Note that the samples AFM1 and AFM4 have the same number of layers, but the first is consisted of mG only, not PEDOT:PSS/mG. It should not be forgotten that the variations in the images are on the order of nanometers, so the films can be considered homogeneous. Furthermore, adding more layers seems to make the films more compact and uniform.

Figure 4e shows another morphological image of the AFM4 sample, away from the step and with higher magnification, where it is possible to notice uniformity of the film, once again. A phase image

(Figure 4f) is collected from the same area, which allows us to draw some conclusions about the film. Phase images of PEDOT:PSS films present light regions associated to the PEDOT-rich regions (more rigid) and dark regions, to the PSS-rich regions (softer) [29,30,34,35,51,53]. On the other hand, in graphene/PEDOT:PSS composite films [29,34], the third component is not easily discernible, however the occurrence of an uniform phase image may indicate film densification, which increases conductivity [53]. Thus, the AFM results help to explain the sheet resistance results, indicating that the performance is linked to the extension and the interconnectivity of the graphene-rich (lighter) and PEDOT-rich (lighter) regions, which form the conductive medium. The dark regions are likely to be non-conducting PSS-rich regions. Therefore, once the existing dark regions do not interfere with the continuousness of the light regions, decrease of the resistance is favored.

4. CONCLUSIONS

In this work, the production and characterization of PEDOT:PSS/mG composites were demonstrated.

The transmittance and sheet resistance results qualify the materials presented here to be used as TCEs, in applications such as OLEDs and OPVs.

Raman spectroscopy showed that the redispersion with the aid of HAc and PEI in IPA incremented the mG concentration reaching 10 mg/mL in IPA, without significant changes in the Raman spectrum of the films, indicating that no significant defects were introduced and that there were no agglomeration of the nanomaterial. In addition, the composites presented the bands observed in the mG spectrum.

Sheet resistances of the composite films decreased by 6 orders of magnitude from those of mG films only, while they are just ca. one half of those found for the PEDOT:PSS films. The properties were correlated to the composition and structure of the materials, raising the hypothesis that the strong π - π interactions between graphene and PEDOT and the transfer of electrons from PEDOT to graphene contribute to the cohesiveness of the film and increases the number of charge carriers and mobility, therefore the composite present higher conductivity.

The thicknesses of the films were estimated by AFM, and the results have shown that depositing additional layers makes the films more compact and uniform, which is also beneficial for reducing the resistance. Furthermore, the phase image compared to the morphological image shows that there are soft regions, corresponding to the PSS-rich domains, and more rigid regions, comprised mainly by PEDOT and mG, showing once again the formation of a composite having interconnected conductive domains.

ACKNOWLEDGMENTS

We thank the Brazilian Coordination for the Improvement of Higher Education Personnel (CAPES, finance code 001) and the Brazilian Council for Scientific and Technological Development (CNPq 306212/2018-8) for financial support and the Nacional de Grafite LTDA (Brazil) for donation of the pristine graphite (99.6%). We also thank M.Sc. Igor Yamamoto Abê for the assistance to acquire Raman spectra, Dr. Daniel Luiz Rodrigues Júnior for the SEM images. We are grateful to the "Laboratório de Filmes Finos do Instituto de Física da Universidade de São Paulo", Brazil, for AFM images.

REFERENCES

- [1] H. Jang; MS Kim; W. Jang; H. Son and DH Wang, *J. of Industrial and Engineering Chemistry*, **86**, 205 (2020).
- [2] R. Fischer; A. Gregori; S. Sahalkalkan; D. Hartmann; P. Büchele; SF Tedde and O. Schmidt, *Organic Electronics* **62**, 351 (2018).
- [3] AK Sarker; J. Kim; B.-H. Wee; H.-J. Song; Y. Lee; J.-D. Hong and C. Lee, *RSC Adv.* **5**, 52019 (2015).
- [4] G. Liu; Y. Liu; M. Zhang; Z. Yang and P. Gane, *Organic Electronics* **81**, p. 105674. (2020).
- [5] J. Saghaei; F. Ali and T, Saghaei, *Organic Electronics* **24**, 188 (2015).
- [6] F. Zabih; Y.Xie; S. Gao and M. Eslamian, *Applied Surface Science* **338**, 163 (2015).
- [7] J. Ouyang, *Displays*, **34**, 423 (2013).
- [8] C.-K. Cho; W.-J. Hwang; K. Eun; S.-H. Choa; S.-I. Na and H.-K. Kim, *Solar Energy Materials & Solar Cells*, **95**, 3269. (2011).
- [9] J. Gasiorowski; R. Menon; K. Hingeri; M. Dachev and NS Sariciftci, *Thin Solid Films*, **536**, 211 (2013).
- [10] SH Chang; W.-N. Chen; C.-C. Chen; S.-C. Yeh; H.-M. Cheng; Z.-L. Tseng; L.-C. Chen; KY Chiu; W.-T. Wu; C.-T. Chen, S.-H. Chen, and C.-G. Wu, *Solar Energy Materials & Solar Cells*, **161**, 7 (2017).
- [11] CS Pathak; JP Singh and R. Singh, *Chemical Physics Lett.* **694**, 75 (2018).
- [12] NA Sarkhan; ZA Rahman; A. Zakaria and AMM Ali, *Materials Today: Proceedings*, **17**, 484 (2019).
- [13] DP Kepić; ZM Marković; SP Jovanović; DV Peruško; MD Budimir; HDI Antunović; VB Pavlović, BMT Marković, *Synthetic Metals* **198**, 150 (2014).
- [14] MJ Allen, VC Tung and RB Kaner, *Chem. Rev.*, **110**, 132. (2010).
- [15] AK Geim and KS Novoselov, *Nature Materials*, **6**, 183. (2007).
- [16] AH Neto; F. Guinea; NMR Peres; KS Novoselov; and AK Geim, *Reviews of modern physics* **81**, 109. (2009).
- [17] F. Bonaccorso; Z. Sun.; T. Hasan and AC Ferrari, *Nature Photonics* **4**, 611 (2010).
- [18] M. Lotya; PJ King; U. Khan; S. De and JN Coleman, *ACS Nano* **4**, 3155 (2010).
- [19] X. You; Q. Feng; J. Yang; K. Huang; J. Hu; S. Dong, *J. Nanopart. Res.* **21**, 19 (2019).
- [20] W. Hong; Y. Xu; G. Lu; C. Li and G. Shi, *Electrochemistry Communications*, **10**, 1555 (2008).
- [21] M. Hilal and JI Han, *Synthetic Metals* **245**, 276 (2018).
- [22] C. Park; D. Yoo; S. Im; S. Kim; W.Cho; J. Ryu and JH Kim, *RSC Adv.* **7**, 25237 (2017).
- [23] J. Santos, *Preparation of graphene through liquid phase exfoliation and nanocomposite semiconductor thin films*, Depto. Eng. Metal. Materials, Polytechnic School, University of São Paulo, São Paulo (2019)
- [24] R. Matroniani; FT Mabilia; JS Santos and SH Wang, *Journal of the Brazilian Chemical Society*, submitted in 2022, (2022)
- [25] C. Casiraghi; A. Hartschuh; H. Qian; S. Piscanec; C. Georgi; A. Fasoli; KS Novoselov; DM Basko; AC Ferrari; *Nano Lett.* **9**, 1433 (2009).
- [26] LG Cañado; A. Jorio; EHM Ferreira; F. Stavale; CA Achete; RB Capable; MVO Moutinho; A. Lombardo; TS Kulmala; AC Ferrari; *Nano Lett.* **11**, 3190 (2011).
- [27] AK Singh; V. Chaudhary; AK Singh; SRP Sinha; *RSC Advances*, **11**, 3096 (2021).
- [28] S. Sanchez-Cortes; RM Berenuel; A. Madejon and M. Pérez-Mendez, *Biomacromolecules* **3**, 655 (2002).
- [29] Y. Seekaew; S. Lokavee; D. Phokharatkul; A. Wisitorsaet; T. Kerdcharoen and C. Wongchoosuk, *Organic Electronics* **15**, 2971 (2014).
- [30] PG Raj; VS Rani; A. Kanwat and J. Jang, *Materials Research Bulletin* **74**, 346 (2016).

- [31] SH Chang; C.-H. Chiang; F.-S. Kao; CL. Tien and CG. Wu, *IEEE Photonics Journal* **6**, 8400307 (2014).
- [32] AA Farah; SA Rutledge; A. Schaarschmidt; R. Lai; JP Freedman and AS Helmy, *Journal of Applied Physics* **12**, 113709 (2012).
- [33] JM Alia; HGM Edwards and BM Kiernan, *Spectrochimica Acta Part A* **60**, 1533, (2004).
- [34] B. Huang; X. Luo; Q. Zou; S. Wang and d J. Zhang, *RSC Adv.* **9**, 42335 (2019).
- [35] D. Jucius; A. Lazauskas; V. Grigaliunas; A. Guobiene; I. Proscivevas; B. Abakeviciene and M. Andrulevicius, *Materials Research* **22**, e20190134 (2019).
- [36] D. Yoo; J. Kim and JH Kim, *Nano Research* **7**, 717 (2014).
- [37] B. Brennan; SJ Spencer; NA Belsey; T. Faris; H. Cronin; SRP Silva; IS Gilmore; Z. Stoeva and AJ Pollard, *Applied Surface Science* **403**, 403 (2017).
- [38] I. Borazan; AC Bedeloglu and A. Demir, *Polymers and Polymer Composites* **28** (1), 66 (2020).
- [39] S. Yoshida "PEDOT:PSS-based polymeric systems for application as device circuits and electrodes", Dept. Eng. Metal. Materials, Polytechnic School of the University of São Paulo, São Paulo (2015)
- [40] H. Chang; G. Wang; A. Yang; X. Tao; X. Liu; Y. Shen and Z. Zheng, *Adv. Function Mater.* **20**, 2893 (2010).
- [41] F. Soltani-kordshuli; F. Zabihi and M. Eslamian, *Engineering Science and Technology, an International Journal* **19**, 1216 (2016).
- [42] S. Khasim; A. Pasha; N. Badi; M. Lakshmi and YK Mishra, *RSC Adv.* **10**, 10526 (2020).
- [43] M. Zhang and JTW Yeow, *Carbon* **156**, 339 (2020).
- [44] L. Wan; B. Wang; S. Wang; X. Wang; Z. Guo; B. Dong; L. Zhao; J.Li; Q. Zhang and T. Luo; *J. Mater. Sci.* **50**, 2148 (2015).
- [45] GH Kim; DH Hwang and SI Woo, *Phys. Chem. Chem. Phys.* **14**, 3530 (2012).
- [46] C. Redondo-Obispo; TS Ripolles; S. Cortijo-Campos; AL Alvarez; E. Climent-Pascual; A. de Andrés and C. Coya, *Materials and Design* **191**, 108587 (2020).
- [47] DS Hecht; L. Hu and G. Irvin, *Adv. Mater.* **23**, 1482 (2011).
- [48] Z. Li; X. Zhang; L. Shen; Z. Fan; X. Chen; M. Chen; S. Qiu; F. Zabihi; M. Eslamian and Q. Chen; *J. Coat. Technol. Res.* **16** (6), 1773 (2019).
- [49] M. Uz; K. Jackson; MS Donta; J. Jung; MT Lentner; JA Hondred; JC Claussen and SK Mallapragada, *Scientific Reports* **9**, 10595 (2019).
- [50] X. Fang; Z. Fan; Y. Gu; J. Shi; M. Chen; X. Chen; S. Qiu; F. Zabihi; M. Eslamian and Q. Chen, *J. Shanghai Jiao Tong Univ. (Sci.)* **23** (1), 106 (2018).
- [51] HS Dehsari; EK Shalamzari; JN Gavgani; FA Taromi and S. Ghanbary, *RSC Adv.* **4**, 55067 (2014).
- [52] A. Hasani; HS Dehsari; JN Gavgani; EK Shalamzari; A. Salehi; FA Taromi and M. Mahyari, *Microchim Acta* **182**, 1551 (2015).
- [53] X. Wang; AKK Kyaw; C. Yin; F. Wang; Q. Zhu; T. Tang; PI Yee and J. Xu, *RSC Adv.* **8**, 18334 (2018).

Nanomaterials Science & Engineering (NMS&E), Vol.4, No.1, 2022

**Department of Mechanical Engineering
University of Aveiro
Aveiro 3810-193
Portugal**

<https://proa.ua.pt/index.php/nmse/>

ISSN: 2184-7002